Nonlinear Coupling of Kinetic Alfvén Waves and Ion Acoustic Waves in the inner Heliosphere

Mani K Chettri[1], Vivek Shrivastav[1], Rupak Mukherjee[1], Nidhi Gaur[2], R. P. Sharma[3]and Hemam D. Singh[1]

[1]Department of Physics, Sikkim University, Gangtok, Sikkim, India
[2]DAV Public School, Sector 14, Gurugram, Haryana, India
[3]Plasma Simulation Laboratory, Department of Energy Science and Engineering, Indian Institute of Technology Delhi, India

Key Points:

- Numerical simulations of modified Zakharov System of Equations satisfied by kinetic Alfvén waves and ion acoustic waves
- Formation of magnetic coherent structures and turbulent spectra
- Flattening of the particle distribution function showing the plasma heating

Corresponding author: Hemam D. Singh, hdsingh@cus.ac.in

Abstract

We study the nonlinear coupling of kinetic Alfvén waves with ion acoustic waves applicable to the Earth's radiation belt and near-Sun streamer belt solar wind using dynamical equations in the form of modified Zakharov systems. Numerical simulations show the formation of magnetic field filamentary structures associated with density humps and dips which become turbulent at later times, redistributing the energy to higher wavenumbers. The magnetic power spectra exhibit an inertial range Kolmogorov-like spectral index value of $-5/3$ for $k_\perp \rho_i < 1$, followed by a steeper dissipation range spectra with indices ~ -3 for the radiation belt case and ~ -4 for the near-Sun streamer belt solar wind case, here $k_\perp$ and ρ_i represent the wavevector component perpendicular to the background magnetic field and the ion gyroradius, respectively. Applying quasilinear theory in terms of the Fokker-Planck equation in the region of wavenumber turbulent spectra, we find the particle distribution function flattening in the superthermal tail population which is the signature of particle energization and plasma heating.

1 Introduction

One of the outstanding problems in solar physics is the heating of the solar corona up to million Kelvin (K), much greater than the Sun's inner surfaces, photosphere ($\approx$ 5700 K) and chromosphere ($\approx$ 50,000 K) allowing the direction of energy flow opposite to the temperature gradient unlike the usual modes of energy transportation via convection, conduction and radiation. In the Earth's magnetosphere also the transfer of energy stored in the magnetotail into the low altitudes of the Earth's atmosphere remains unresolved. The magnetic reconnection and wave-heating models (Fisk, 2003; McComas et al., 2007; Velli et al., 2015) are broadly accepted mechanisms for energy conversion in space and the magnetospheric plasmas. Many theoretical studies have shown that in a magnetized plasma environment, Alfvén waves can heat the plasma via wave dissipation (Del Zanna & Velli, 2002; Escande et al., 2019) and accelerate the solar wind through the action of wave pressure (Alazraki & Couturier, 1971; Suzuki & Inutsuka, 2006). These theories are supported by many spacecraft observations showing various signatures of Alfvénic perturbations in the photosphere (Song & Vasyliūnas, 2011) and chromosphere of the Sun (Grant et al., 2018), solar coronal regions (Sharma Pyakurel et al., 2018; Kasper et al., 2021) and solar wind flowing at various regions of the heliosphere(C. C. Chaston et al., 2000, 2005; Raghav & Kule, 2018; Kasper et al., 2021; D'Amicis, Bruno, et al., 2021; D'Amicis, Perrone, et al., 2021). These observations not only corroborate the existence of Alfvén waves but also quantify their energy contributions to the coronal heating problem and solar wind acceleration (McComas et al., 2007; Chae et al., 2021), bridging theoretical predictions with empirical evidence.

The magnetohydrodynamic (MHD) Alfvén waves become dispersive when the transverse spatial length scale (wavelength) is comparable to the electron inertial scale (Goertz & Boswell, 1979) or the ion gyroradius (Stéfant, 1970; Hasegawa, 1976). Dispersive Alfvén waves can be classified into two categories, kinetic and inertial depending on specific local plasma properties (N. Shukla et al., 2009; Rai et al., 2017; Barik et al., 2021). If the electron thermal speed is greater than the local Alfvén speed (v_A), the wave is kinetic that is valid in hot plasma having $\beta_e \gg m_e/m_i$, where β_e ($= 8\pi n_e T_e/B_0^2$) is the ratio of the electron thermal pressure to the magnetic pressure, m_e (m_i) is the mass of electron (ion), n_e is the electron density, T_e is the electron temperature, B_0 is the background (ambient) plasma magnetic field. If the electron thermal speed is less than v_A, the wave is inertial which is valid for cold plasma having $\beta_e \ll m_e/m_i$. These two kinds of dispersive Alfvén waves are commonly known as kinetic Alfvén waves (KAWs) that can be differentiated by high β and low β. They retain some basic properties of MHD Alfvén waves such as currents along the magnetic field lines and quasi-parallel group velocity. However, the ions no longer follow the ambient magnetic field lines but the electrons follow it due to the smaller gyroradius when the wave dynamics are faster than the ion or-

bital motions (Hasegawa, 1976; Johnson & Cheng, 1997; Hollweg, 1999). These unmatched motions between electrons and ions develop charge separation generating a parallel electric field that can heat plasma particles along the ambient magnetic field lines (Tsiklauri, 2006; Cheng et al., 2016).

The existence of KAWs can be identified by measuring the ratio of electric and magnetic field fluctuations perpendicular to the background magnetic field ($\delta E_\perp/\delta B_\perp$), calculated from the spectra of satellite observations and comparing it with the theoretical predictions (L. Chen et al., 2021). For long wavelength shear Alfvén waves, this ratio is v_A. By analyzing the Parker Solar Probe (PSP) spacecraft data during its first near-Sun encounter, Malaspina et al. (2022) showed that the ratio is greater than v_A for low frequency ≈ 1 Hz, matching with the theoretical prediction calculated by Stasiewicz et al. (2000) by combining the dispersion relation and polarisation properties of KAWs in the low frequency limit ($\omega \ll \omega_{ci}$) as

$$\frac{|\delta E_\perp|}{|\delta B_\perp|} = \frac{v_A\left(1+k_\perp^2\rho_i^2\right)}{\sqrt{1+k_\perp^2\left(\rho_s^2+\rho_i^2\right)}}, \tag{1}$$

where ω is the frequency of the pump KAW, ω_{ci} is the ion gyro-frequency, $\rho_i = v_{ti}/\omega_{ci}$ is the ion gyroradius, v_{ti} $(= \sqrt{\gamma_i k_B T_i/m_i}$ is the thermal speed of ion, $\rho_s = v_{te}/\omega_{ci}$ is the proton gyroradius, v_{te} $(= \sqrt{\gamma_e k_B T_e/m_e})$ is the thermal speed of electron, $\gamma_e(\gamma_i)$ is the ratio of specific heats $(c_p/c_v$) for electrons (ions), and $k_\perp$ represents the wavevector component perpendicular to the background magnetic field direction. At frequencies, $\omega > \omega_{ci}$, the discrepancies between the theoretical and observational values of $\delta E_\perp/\delta B_\perp$ arise which may be due to the observations reaching the noise level of the instruments and as well as non inclusion of the additional terms like $\left(1-\omega^2/\omega_{ci}^2\right)$ in the theory (Salem et al., 2012).

Numerous observational studies from Polar, Cluster, Viking, Freja and Fast Auroral SnapshoT (FAST) spacecraft have provided compelling evidence for the prevalence of KAWs in various regions of the Earth's magnetosphere (Johnson et al., 2001; C. Chaston et al., 2005; Dai, 2009; Duan et al., 2012, 2016). Van Allen Probes measurements have revealed the existence of KAWs in the inner magnetosphere (C. Chaston et al., 2015, 2018), predominantly because of the injections from the magnetotail (Ripoll et al., 2020). Near the Earth's plasma sheet regions, KAWs are excited at the onset of substorm events, resulting from gradients in particle number density and magnetic field strength (Duan et al., 2012). The fluctuating fields of KAWs can have frequencies of $\approx 0.2-20$ Hz in the spacecraft frame (C. Chaston et al., 2012) while the shear Alfvén waves (for which kinetic effects are negligible) can have frequencies $\approx 15-50$ mHz (Keiling et al., 2005; Zhang et al., 2022). Earlier observations of KAWs mostly occurred in the solar wind at 1 AU within a frequency range slightly beyond or less than ten times the ion gyro-frequency. Most recently, the PSP has reached 0.0485 AU distance from the Sun's centre as of September 27, 2023 (Johns Hopkins University Applied Physics Laboratory, 2023), providing us to test whether solar wind electromagnetic fluctuations exhibit KAW properties at frequencies extending well beyond the ion gyro-frequency range. To investigate the presence of higher frequency whistler modes, the ratio of the magnetic field fluctuations along the ambient magnetic field ($\delta B_\parallel$) to the fluctuations of the total magnetic field (δB) were evaluated from the observational spectra, as a function of frequency (Shaikh & Zank, 2009; C. C. Chaston et al., 2009). It confirmed the dominance of KAWs at 1 AU over whistler mode below the gyroscale (Bale et al., 2005; Sahraoui et al., 2010). In the near-Sun solar wind, Malaspina et al. (2022) calculated this ratio by analyzing the PSP spacecraft data and found that at low frequency, the ratio is small, then increases until the frequency where the Alfvén waves become dispersive, then remains constant below 1. All these characteristics support the presence of KAW fluctuations in the near-Sun solar wind. Because of the KAW fluctuations, the turbulent energy is dissipated spatially inhomogeneous to heat the plasma. This evidence can be used as a model to study how the KAW turbulence fits into the macroscopic scales such as solar wind, particle acceleration and ener-

gization of the plasma through dissipation. Several theoretical models, such as phase mixing (Heyvaerts & Priest, 1983), turbulent cascade (Matthaeus et al., 1999) and resonant absorption (Goossens et al., 2011) have been proposed to understand the dissipation mechanism in the solar wind. Although there is no generally agreed mechanism due to variations in dissipation rates, length scales and the physics involved.

The solar corona is categorized into inner, middle and outer regions, each with distinct magnetic field lines and plasma dynamics. The inner corona features closed magnetic fields and plasma $\beta < 1$, transitioning to open fields and higher β values in the middle region. The PSP provides us adequate data to analyze the plasma properties in sub-Alfvénic and super-Alfvénic flows covering many solar regions of low, intermediate and high β plasmas (Larosa, 2021; Zhao, Zank, Telloni, et al., 2022). Inhomogeneities within the inner corona suggest that pure Alfvén modes cannot propagate effectively, leading to alternative dissipation mechanisms like phase mixing and resonance. KAWs are considered a key heating mechanism, though their efficiency and interaction details are not fully understood, partly due to observational challenges in determining KAWs' spatial structures. The Magnetospheric Multiscale (MMS) Mission data analysis reveals KAWs' perpendicular wavelengths are about 2.4 times the ion gyroradius (Liu et al., 2023). Some studies (Lysak et al., 1980; C. Chaston et al., 2004; Shen & Knudsen, 2020) suggested that it is difficult to produce particles with gyroradius larger than the perpendicular wavelength ($\lambda_\perp$) of the waves. This condition sets the maximum proton perpendicular energy as $\lesssim eB_0\lambda_\perp^2/2m_p$, resulting it to be 5.76 times the proton perpendicular thermal energy in coherent structures with KAWs. Through stochastic heating, the plasma particles can attain more energy than as given by this restriction (Lysak et al., 1980; C. Chaston et al., 2004; Shen & Knudsen, 2020).

Previous studies, including observations by PSP and Solar Orbiter, have unveiled a broad power spectrum in turbulent solar wind fluctuations, spanning timescales from several hours down to approximately 0.01 seconds in spacecraft reference frames (Alexandrova et al., 2013; Telloni et al., 2021; Šafránková et al., 2023). Using MHD turbulence theory reveals that magnetic field spectra in the inertial range is predominantly oriented perpendicular to the mean magnetic field direction (Bale et al., 2005; L. Chen et al., 2011). Specifically, the spectral index at 1 AU approaches $\approx -5/3$ in the inertial range, gradually steepening to spectral indices between -2 and -4 at smaller kinetic scales (Alexandrova et al., 2009; L. Chen et al., 2013; L. Chen & Zonca, 2016). Similar trends of $-5/3$ in the inertial range and much steeper at the kinetic scale were also reported from PSP observations (C. H. K. Chen et al., 2020; Shi et al., 2021; Šafránková et al., 2023; Lotz et al., 2023). In the dissipation range, Šafránková et al. (2023) found a spectral index of -4.8 at the closest approach (0.12 AU) to the Sun then becoming flatter as it moves away, approaching it ≈ -3 at around 0.4 AU. From 0.4 AU to 1 AU, the spectral indices remain approximately constant ($-5/3$ at inertial and ≈ -3 at dissipation range).

Our present work focuses on the nonlinear interactions of KAWs and ion acoustic waves applicable for an arbitrary β plasma (both $\beta < 1$ and $\beta > 1$) by taking the non-adiabatic response of the background density in the presence of nonlinear ponderomotive force. For this purpose, we have derived the model equations in the form of generalized Zakharov equations, called here as modified Zakharov System of Equations (modified ZSEs). The equations were solved numerically to understand the solar wind turbulence near the Earth and the Sun. The numerical simulation results showed coherent magnetic filamentary structures of KAWs associated with density humps and dips becoming turbulent as time evolves indicating the redistribution of energy among the higher wavenumbers. Many authors (P. K. Shukla et al., 2004; H. Singh & Sharma, 2006; Kumar et al., 2009; Yadav & Sharma, 2014; H. D. Singh & Jatav, 2019) have studied the wave turbulence generated because of the interaction of KAWs and ion acoustic waves by taking the adiabatic and non-adiabatic response of the background density. However, all these studies were limited only to low $\beta < 1$. Recently, I. Singh et al. (2022) and

Dewan et al. (2022) studied the magnetic turbulence applicable for arbitrary β plasma when the pump KAWs interact with low magnetosonic waves (I. Singh et al., 2022) and high-frequency oblique whistler waves (Dewan et al., 2022) to understand the role of plasma β in the laboratory and astrophysical plasmas. Although they have used the model applicable to all the ranges of plasma β, they have considered high $\beta \sim 100$ for the sake of illustration only without applying it to any real laboratory or space plasma environments. Moreover, these studies were limited to the situations where KAW frequency is much less than the ion cyclotron frequency. In this paper, we have considered the coupling of pump KAWs and ion acoustic waves (and rederived the model equations when KAW frequency is not necessarily less than ion cyclotron frequency) for $\beta \approx 0.0041$ and $\beta \approx 6.940$ applicable for near the Earth radiation belt and near-Sun streamer belt solar wind, respectively. The framework of the present paper is organized as follows: the model equations in the form of modified ZSEs are derived in section 2, the numerical simulation results are presented in section 3, the particle heating as evident from the super thermal tail expansion of the distribution function is examined in section 4, finally, section 5 summarizes the overall results of the present investigation.

2 Model Equations

2.1 Dynamics of Pump KAW

We consider a collisionless, non-relativistic two-fluid (electrons and protons as ions) magnetoplasma having a uniform background magnetic field $\mathbf{B_0} = (0, 0, B_0)$ and the electric field $\mathbf{E} = \delta\mathbf{E}$, where $\delta\mathbf{E}$ is the fluctuating component. In our geometry, the $z-$direction is parallel to $\mathbf{B}_0$ and the pump KAW propagates in the $x-z$ plane such that the wavevector $\mathbf{k_0} = k_{0x}\hat{x}+k_{0z}\hat{z}$, where all the wave variations are in the $x-z$ plane, i.e., $(\partial/\partial x, 0, \partial/\partial z)$, except the induced magnetic field perturbations in the $y-$direction (δB_y). The directions along and across $\mathbf{B_0}$ are denoted as parallel and perpendicular directions respectively. The linearized continuity and momentum equations are

$$\frac{\partial \delta n_s}{\partial t} + n_{0s}\nabla \cdot \delta \mathbf{v_s} \approx 0 \tag{2}$$

and

$$m_s \frac{\partial \delta \mathbf{v_s}}{\partial t} \approx q_s \delta \mathbf{E} + \frac{q_s}{c}(\delta \mathbf{v_s} \times \mathbf{B_0}) - \frac{\gamma_s k_B T_s}{n_{0s}} \nabla \delta n_s \tag{3}$$

respectively, where s indicates the species of the particles: electrons (e) and ions (i), m_s, q_s, T_s, n_{0s} represent the mass, charge, temperature and average density of the species s respectively; c is the speed of light, δn_s is the fluctuation in number density, $\delta \mathbf{v_s}$ is the bulk velocity ($\mathbf{v} = \delta \mathbf{v_s}$, with no mean flow velocity), γ_s is the ratio of specific heats (c_p/c_v) and k_B is the Boltzmann constant. Additionally, we assume quasineutrality condition: $n_{0e} \simeq n_{0i} \simeq n_0$ and $\delta n_e \simeq \delta n_i \simeq \delta n$ in both equilibrium and perturbed state, the isothermal condition: $\gamma_e = \gamma_i = 1$ and small perturbations: $\delta n_s/n_{0s} \ll 1$ and $\delta B_y/B_0 \ll 1$. It may be mentioned here that in deriving the linearized equations we have neglected the nonlinear term $(\mathbf{v}.\nabla)\mathbf{v}$ in the convective derivative $(\partial/\partial t+\mathbf{v}.\nabla)$, valid for weak dispersion to avoid the vector nonlinearity (Sadiq et al., 2018a). Even if it is not for weak dispersion, the convective term can be neglected for the perpendicular motion (Kaur & Saini, 2016; Sadiq et al., 2018a; M. Singh et al., 2021).

From equation (3), assuming all the first order fluctuations to be of the form of $\delta f = \delta f e^{i(k_{0x}x+k_{0z}z-\omega t)}$, where ω is the frequency of the pump KAW, we can separate the electron and ion velocity components, respectively, as

$$\delta v_{ex} = \frac{1}{\omega_{ce}^2 - \omega^2}\frac{e}{m_e}\left(i\omega\delta E_x + \omega_{ce}\delta E_y + i\omega\frac{\gamma_e k_B T_e}{n_0 e}\frac{\partial \delta n}{\partial x}\right), \tag{4}$$

$$\delta v_{ey} = \frac{e\delta E_y}{\omega_{ce}^2 - \omega^2}\frac{i\omega}{m_e} - \frac{e}{m_e}\frac{\omega_{ce}}{\omega_{ce}^2 - \omega^2}\left(\delta E_x + \frac{\gamma_e k_B T_e}{n_0 e}\frac{\partial \delta n}{\partial x}\right), \tag{5}$$

$$\delta v_{ez} = \frac{e\delta E_z}{m_e}\frac{1}{i\omega} + \frac{1}{i\omega}\frac{\gamma_e k_B T_e}{n_0 m_e}\frac{\partial \delta n}{\partial z}, \tag{6}$$

$$\delta v_{ix} = \frac{e}{m_i}\frac{1}{\omega_{ci}^2 - \omega^2}\left(\omega_{ci}\delta E_y - i\omega\left(\delta E_x - \frac{\gamma_i k_B T_i}{n_0 e}\frac{\partial \delta n}{\partial x}\right)\right), \tag{7}$$

$$\delta v_{iy} = -\frac{e}{m_i}\frac{\omega_{ci}}{\omega_{ci}^2 - \omega^2}\left(i\frac{\omega\delta E_y}{\omega_{ci}} + \delta E_x - \frac{\gamma_i k_B T_i}{n_0 e}\frac{\partial \delta n}{\partial x}\right) \tag{8}$$

and

$$\delta v_{iz} = -\frac{e\delta E_z}{m_i}\frac{1}{i\omega} + \frac{1}{i\omega}\frac{\gamma_i k_B T_i}{n_0 m_i}\frac{\partial \delta n}{\partial z}, \tag{9}$$

where $\omega_{ce} = eB_0/m_e c$ is the electron cyclotron frequency and $\omega_{ci} = eB_0/m_i c$ is the ion cyclotron frequency.

The electron and ion continuity equations can be respectively written as

$$\frac{\partial \delta n_e}{\partial t} + n_0\left(\frac{\partial \delta v_{ex}}{\partial x} + \frac{\partial \delta v_{ez}}{\partial z}\right) = 0, \tag{10}$$

and

$$\frac{\partial \delta n_i}{\partial t} + n_0\frac{\partial \delta v_{ix}}{\partial x} = 0. \tag{11}$$

In writing equation (11), we neglected the parallel ion motion because of the larger mass and Larmor radius, its motion spends much of the time in the perpendicular direction.

From equation (10), neglecting the perpendicular electron motion due to its small polarization drift velocity because of small mass and Larmor radius, we get

$$\delta n_e = \frac{n_0 k_{0z}}{\omega}\delta v_{ez}, \tag{12}$$

and substituting it into equation (6) we get

$$\delta v_{ez} = \frac{e\delta E_z}{i\omega m_e} + \left(\frac{\gamma_e k_B T_e}{m_e}\right)\frac{k_{0z}^2}{\omega^2}\delta v_{ez}. \tag{13}$$

Using the dispersion relation of shear Alfvén wave $v_A = \omega/k_{0z}$, the ion acoustic speed $c_s = \sqrt{k_B(\gamma_e T_e + \gamma_i T_i)/m_i}$ with the isothermal condtions, $\gamma_e = \gamma_i$ and $T_e = T_i$, and denoting plasma β as $(c_s^2/2v_A^2)$, the above equation (13) becomes

$$\frac{m_e}{m_i}\delta v_{ez} = \frac{e\delta E_z}{i\omega m_i} + 2\beta\delta v_{ez}. \tag{14}$$

In equation (14), if we consider only for plasma $\beta \gg (m_e/m_i)$, the left-hand side representing the electron inertial term can be neglected. Since our study is based on any arbitrary β we will retain this term.

Using the Faraday's law

$$\nabla \times \mathbf{E} = -\frac{1}{c}\frac{\partial \mathbf{B}}{\partial t} \tag{15}$$

and taking $y-$ component and differentiating w.r.t. $'t'$, we get

$$\frac{\partial^2(\delta B_y)}{\partial t^2} = c\frac{\partial^2(\delta E_z)}{\partial t \partial x} - c\frac{\partial^2(\delta E_x)}{\partial t \partial z}. \tag{16}$$

To obtain the dynamical equation satisfied by the transverse perturbed magnetic fields of the pump KAWs, first, we will express the perpendicular and parallel perturbed electric fields δE_x and δE_z respectively in terms of δB_y. Subtracting electron and ion continuity equations, and using the quasineautrality condition, we get the conservation law of current density as

$$\nabla \cdot \mathbf{J} = 0, \tag{17}$$

where the current density $\mathbf{J} = en_0\left(\delta\mathbf{v_i} - \delta\mathbf{v_e}\right)$.

In velocity components form the above equation can be written as

$$en_0\left(\frac{\partial\left(\delta v_{ix}\right)}{\partial x} - \frac{\partial\left(\delta v_{ex}\right)}{\partial x} - \frac{\partial\left(\delta v_{ez}\right)}{\partial z}\right) = 0. \tag{18}$$

Substituting the expressions for $\delta v_{ex}, \delta v_{ez}$ and δv_{ix} given by the equations (4), (6) and (7), and using $\frac{\partial}{\partial t} \rightarrow (-i\omega)$, the above equation is transformed to

$$\frac{\partial^2\left(\delta E_x\right)}{\partial t \partial x} = -\frac{\partial\left(\delta E_y\right)}{\partial x}\omega_{ci} + \left(\omega_{ci}^2 - \omega^2\right)\frac{m_i}{e}\frac{\partial\left(\delta v_{ez}\right)}{\partial z}. \tag{19}$$

We can write the Ampere's law as

$$\nabla \times \mathbf{B} = \frac{4\pi}{c}\mathbf{J}, \tag{20}$$

here we have neglected the displacement current because of the low frequency assumption, $\omega \ll \omega_{pe}$, where ω_{pe} is the electron plasma frequency expressed as $\sqrt{4\pi n_0 e^2/m_e}$. In such a situation, the phase velocity of the wave is much smaller than the speed of light. If we assume the characteristic time and the length scales as τ and l respectively, then $\partial/\partial t \sim \tau^{-1}$, $\nabla \sim l^{-1}$ and phase velocity $v_{ph} \sim l/\tau$. Again, Faraday's law gives the scaling $\frac{E}{B} \sim \frac{v_{ph}}{c}$. Now, comparing the magnitudes of the displacement current and the left-hand side of equation (20), we get $\frac{\partial \mathbf{E}/\partial t}{c\nabla\times\mathbf{B}} \sim \frac{\mathbf{E}/\tau}{c\mathbf{B}/l} \sim \frac{v_{ph}^2}{c^2} \ll 1$ as $v_{ph} \ll c$.

Taking the $z-$component of equation (20) and differentiating it w.r.t. $'t'$, we get

$$\frac{\partial^2\left(\delta B_y\right)}{\partial t \partial x} = \frac{4\pi}{c}\frac{\partial J_z}{\partial t}. \tag{21}$$

Here, the parallel component of the current density is entirely carried by the electron's motion i.e., $J_z = -en_e\delta v_{ez}$. Substituting the expression for J_z along with $n_e = n_0 + \delta n$, we get

$$\frac{\partial^2\left(\delta B_y\right)}{\partial t \partial x} = \frac{\omega_{pe}^2}{c}\left(1 + \frac{\delta n}{n_0}\right)\left(\delta E_z + \frac{\gamma_e k_B T_e}{en_0}\frac{\partial\left(\delta n\right)}{\partial z}\right). \tag{22}$$

The parallel component of the electric field can be written from equation (22) as

$$\delta E_z = \frac{c}{\omega_{pe}^2}\frac{\partial^2\left(\delta B_y\right)}{\partial t \partial x}\left(1 - \frac{\delta n}{n_0}\right) - \frac{\gamma_e k_B T_e}{en_0}\frac{\partial\left(\delta n\right)}{\partial z}. \tag{23}$$

This expression for δE_z can be used to find out $\delta v_{ez}/\partial z$ from equation (6) to get

$$\frac{\partial\left(\delta v_{ez}\right)}{\partial z} = \frac{ec}{i\omega}\frac{1}{\omega_{pe}^2 m_e}\frac{\partial^3\left(\delta B_y\right)}{\partial t \partial x \partial z}\left(1 - \frac{\delta n}{n_0}\right). \tag{24}$$

Putting equation (24) into equation (19), we get

$$\frac{\partial\left(\delta E_x\right)}{\partial t} = -\omega_{ci}\delta E_y - \frac{m_i c\left(\omega_{ci}^2 - \omega^2\right)}{m_e\omega_{pe}^2}\frac{\partial\left(\delta B_y\right)}{\partial z}\left(1 - \frac{\delta n}{n_0}\right). \tag{25}$$

The $z-$component of Faraday's law (15) is given as

$$\delta E_y = \left(\omega/ck_{0x}\right)\delta B_z. \tag{26}$$

In the case of low frequency $\omega \ll \omega_{ci}$ and low plasma β approximation, the compressive component of the magnetic field perturbation (δB_z) will play no significant contribution, i.e., we can take $\delta B_z = 0$ (Howes et al., 2006; Schekochihin et al., 2009; Cramer,

2011). However, for arbitrarily finite β consideration, the parallel component of the magnetic field perturbation should be taken into account and can be calculated from the pressure balance equation $\nabla\left(k_B T\delta n_e + \delta B_z^2/8\pi\right) = 0$. This gives $\delta B_z/B_0 = -\beta\delta n_e/2n_0$ which indicates a strong anti-correlation between the magnetic and thermal pressures. It is used to examine the density and magnetic field fluctuations observed in the inertial range of the magnetic field turbulence spectra (Burlaga et al., 1990; Roberts, 1990; Bavassano et al., 2004). Furthermore, by using the continuity equation (2) and Ampere's law (20) we get

$$\delta B_z = -\frac{\beta}{2}\frac{\omega_{ce}c^2}{\omega_{pe}^2}\frac{k_{0x}}{\omega}\frac{\partial\left(\delta B_y\right)}{\partial z}. \tag{27}$$

Substituting equations (26) and (27) into equation (25) and differentiating once w.r.t. $'t'$ we get

$$\frac{\partial^2\left(\delta E_x\right)}{\partial t\partial z} = \frac{\omega_{ci}\beta B_0}{8\pi e n_0}\frac{\partial^2\left(\delta B_y\right)}{\partial z^2} - \frac{v_A^2}{c\omega_{ci}^2}\left(\omega_{ci}^2-\omega^2\right)\frac{\partial^2\left(\delta B_y\right)}{\partial z^2}\left(1-\frac{\delta n_s}{n_0}\right). \tag{28}$$

Differentiating J_z w.r.t. $'t'$ we get

$$\frac{\partial J_z}{\partial t} = n_e e\left(\frac{e\delta E_z}{m_e} + \frac{\gamma_e k_B T_e}{n_e m_e}\frac{\partial\delta n_e}{\partial z}\right). \tag{29}$$

By calculating J_z from Ampere's law (20) and substituting it into equation (29) we get

$$\frac{\partial\left(\delta E_z\right)}{\partial t} = \frac{\lambda_e^2}{c}\frac{\partial^3\left(\delta B_y\right)}{\partial t^2\partial x} - \frac{v_{te}^2\lambda_e^2}{c}\frac{\partial^3\left(\delta B_y\right)}{\partial x\partial z^2} \tag{30}$$

where $\lambda_e = c/\omega_{pe}$ is the electron inertial length.

Differentiating equation (30) w.r.t. $'x'$ and substituting it to equation (16) along with equation (28), we get the following dynamical equation

$$\begin{aligned}&\frac{\partial^2\left(\delta B_y\right)}{\partial t^2} - \lambda_e^2\frac{\partial^4\left(\delta B_y\right)}{\partial t^2\partial x^2} + v_{te}^2\lambda_e^2\frac{\partial^4\left(\delta B_y\right)}{\partial x^2\partial z^2} + \frac{B_0 c\beta\omega_{ci}}{8\pi n_0 e}\frac{\partial^2\left(\delta B_y\right)}{\partial z^2}\\ &- v_A^2\left(\frac{\omega_{ci}^2-\omega^2}{\omega_{ci}^2}\right)\left(1-\frac{\delta n}{n_0}\right)\frac{\partial^2\left(\delta B_y\right)}{\partial z^2} = 0.\end{aligned} \tag{31}$$

By performing the Fourier transform in the linear part of equation (31), we get the linear dispersion relation of KAWs as

$$\frac{\omega^2}{k_{0z}^2} = v_A^2\left(\frac{1+k_{0x}^2\rho_i^2+(\beta/2)}{1+\lambda_e^2k_{0x}^2+\lambda_i^2k_{0z}^2}\right). \tag{32}$$

If we neglect the effect of the finite beta correction, the above dispersion relation of KAWs can be transformed for $m_e/m_i \ll \beta \ll 1$ as $\omega^2 = v_A^2k_{0z}^2\left(1+k_{0x}^2\rho_i^2\right)$ (P. K. Shukla & Stenflo, 2005) in the limit of $\lambda_e k_{0x} \ll 1$ and $\lambda_i k_{0z} \ll 1$.

The dynamical equation (31) is satisfied by the magnetic field perturbations of pump KAWs. One of the possible solutions of equation (31) is a plane wave (linearly polarised) having base frequency ω, modulated by a slowly varying envelope $\delta\tilde{B_y}$ which is expressed as

$$\delta B_y = \delta\tilde{B}_y(x,z,t)\ e^{i(k_{0x}x+k_{0z}z-\omega t)} \tag{33}$$

where $\delta\tilde{B}_y(x,z,t)$ is the inhomogeneous amplitude of the transverse pump KAW magnetic field slowly varying in space in comparison to the exponential part $e^{i(k_{0x}x+k_{0z}z-\omega t)}$.

Substituting equation (33) into (31) we get the envelope equation of the KAWs as

$$
\begin{aligned}
&2i\omega\left(1+\lambda_e^2k_{0x}^2\right)\frac{\partial\left(\delta\tilde{B_y}\right)}{\partial t}+2i\left(k_{0x}\lambda_e^2k_{0z}^2v_{te}^2-k_{0x}\lambda_e^2\omega^2\right)\frac{\partial\left(\delta\tilde{B_y}\right)}{\partial x}\\
&+\left(v_{te}^2\lambda_e^2k_{0z}^2-\lambda_e^2\omega^2\right)\frac{\partial^2\left(\delta\tilde{B_y}\right)}{\partial x^2}+\left[k_{0z}v_{te}^2\lambda_e^2+\frac{cB_0\beta\omega_{ci}}{8\pi n_0e}+v_A^2\left(1-\frac{\omega^2}{\omega_{ci}^2}\right)\right]\frac{\partial^2\left(\delta\tilde{B_y}\right)}{\partial z^2}\\
&+2ik_{0z}\left[v_{te}^2\lambda_e^2k_{0x}^2+v_A^2\left(1-\frac{\omega^2}{\omega_{ci}^2}\right)+\frac{cB_0\beta\omega_{ci}}{8\pi n_0e}\right]\frac{\partial\left(\delta\tilde{B_y}\right)}{\partial z}+4\lambda_e^2k_{0x}\omega\frac{\partial^2\left(\delta\tilde{B_y}\right)}{\partial t\partial x}\\
&-2i\omega\lambda_e^2\frac{\partial^3\left(\delta\tilde{B_y}\right)}{\partial t\partial x^2}-2ik_{0z}v_{te}^2\frac{\partial^3\left(\delta\tilde{B_y}\right)}{\partial x^2\partial z}-v_{te}^2\lambda_e^2\frac{\partial^4\left(\delta\tilde{B_y}\right)}{\partial x^2\partial z^2}-2ik_{0x}v_{te}^2\lambda_e^2\frac{\partial^3\left(\delta\tilde{B_y}\right)}{\partial x\partial z^2}\\
&+4k_{0x}k_{0z}v_{te}^2\lambda_e^2\frac{\partial^2\left(\delta\tilde{B_y}\right)}{\partial x\partial z}+v_A^2k_{0z}^2\frac{\delta n}{n_0}\left(1-\frac{\omega^2}{\omega_{ci}^2}\right)\delta\tilde{B_y}=0.
\end{aligned}
\tag{34}
$$

2.2 Ion Acoustic Wave Dynamics

In a spatially varying wave propagation, a nonlinear force known as ponderomotive force is generated. The ponderomotive force is a time averaged force that acts on charged particles in a nonuniform electromagnetic field. Within a nonuniform, inhomogeneous plasma medium, the combined influence of the ponderomotive force and Joule heating generated from plasma currents, can induce modifications to the plasma density (P. Shukla et al., 1999). In both laboratory and space plasma environments, large amplitude KAWs lead to fluctuations in plasma density, manifesting as humps and dips aligned with the field (Gekelman, 1999; P. Shukla & Stenflo, 2000a, 2000b). These studies focused on the fluctuations of particle density under the adiabatic approximation, wherein the density changes slowly over time relative to density fluctuations. Here, we are considering non-adiabatic variations of particle density under the influence of ponderomotive force represented by the ion acoustic wave dynamics. Let us consider ion acoustic waves propagating along the $z-$direction $\mathbf{k}=k_{0z}\hat{z}$ with magnetic field $\mathbf{B}=B_0\hat{z}+\delta B_y\hat{y}$. The linearized continuity and momentum equations are given respectively as

$$
\frac{\partial\left(\delta n_s\right)}{\partial t}+n_{0s}\frac{\partial\left(\delta v_{sz}\right)}{\partial z}=0 \tag{35}
$$

and

$$
m_s\left(\frac{\partial\left(\delta\mathbf{v_s}\right)}{\partial t}+\delta v_{sz}\frac{\partial\left(\delta\mathbf{v_s}\right)}{\partial z}\right)=q_s\left(\delta\mathbf{E}+\frac{\delta\mathbf{v_s}\times\left(B_0\hat{z}+\delta B_y\hat{y}\right)}{c}\right)-\frac{k_BT_s}{n_{0s}}\frac{\partial\left(\delta n_s\right)}{\partial z}\hat{z}. \tag{36}
$$

Here, only the first-order linearisation in the continuity equation is used, but both the first-order and second-order linearisations are used in the momentum equation. The second-order linearisation is used to obtain the dynamics of the ion acoustic wave due to the ponderomotive effects of the pump KAWs. The ponderomotive force term is

$$
\mathbf{F}_s=\frac{q_s}{c}\left(\delta\mathbf{v}_s\times\delta B_y\hat{y}\right)-m_s\delta v_{sz}\frac{\partial\left(\delta\mathbf{v}_s\right)}{\partial z}, \tag{37}
$$

where the first term is the Lorentz force and the second term is the convective term. The parallel velocity components satisfy the following equation

$$
m_s\frac{\partial\left(\delta v_{sz}\right)}{\partial t}=q_s\delta E_z-\frac{k_BT_s}{n_{0s}}\frac{\partial\left(\delta n_s\right)}{\partial z}+F_{sz}, \tag{38}
$$

where $F_{sz}=\frac{q_s}{c}\left(\delta v_{sx}\delta B_y\right)-m_s\delta v_{sz}\frac{\partial}{\partial z}\delta v_{sz}$ is the parallel component of the ponderomotive force due to the pump KAW. Here, it should be mentioned that the parallel ponderomotive force is dominant over the other perpendicular components. By assuming the massless electrons, we can find out the parallel component of the electric field as

$$
\delta E_z=-\frac{1}{e}\frac{k_BT_e}{n_{0e}}\frac{\partial\left(\delta n_e\right)}{\partial z}+\frac{1}{e}F_{ez}. \tag{39}
$$

Imposing the quasi-neutrality condition, i.e., $n_{0i} = n_{0e} \equiv n_0$ and $\delta n_i = \delta n_e \equiv \delta n$, the continuity equation (35) implies that $\delta v_{iz} = \delta v_{ez}$, hereafter we denote this variable as δv_z. Substituting equation (39) in equation (36), we get

$$\frac{\partial (\delta v_z)}{\partial t} = -\frac{c_s^2}{n_0}\frac{\partial (\delta n)}{\partial z} + \left(\frac{F_{iz} + F_{ez}}{m_i}\right). \tag{40}$$

Differentiating equation (35) w.r.t. 't', we get

$$\frac{\partial^2 (\delta n)}{\partial t^2} + n_0 \frac{\partial^2 (\delta v_z)}{\partial t \partial z} = 0. \tag{41}$$

Substituting equation (40) into equation (41), we get the equation for density fluctuations due to the ponderomotive force of the pump KAW as

$$\frac{\partial^2 (\delta n)}{\partial t^2} + n_0 \frac{\partial}{\partial z}\left[-\frac{c_s^2}{n_0}\frac{\partial (\delta n)}{\partial z} + \frac{F_{iz} + F_{ez}}{m_i}\right] = 0. \tag{42}$$

We rewrite equation (42) as

$$\left(\frac{\partial^2 (\delta n)}{\partial t^2} - c_s^2 \frac{\partial^2}{\partial z^2}\right)\frac{\delta n}{n_0} = -\frac{\partial}{\partial z}\left(\frac{(F_{iz} + F_{ez}}{m_i}\right) \tag{43}$$

Similarly, we can write the equation for δv_z as

$$\left(\frac{\partial^2}{\partial t^2} - c_s^2 \frac{\partial^2}{\partial z^2}\right)\delta v_z = \frac{\partial}{\partial t}\left(F_{iz} + F_{ez}\right). \tag{44}$$

We see that the wave equation (44) involves the time derivative of the ponderomotive forcing term due to the pump KAWs instead of the spatial derivative that appears in the density fluctuation equation (43). Let us evaluate the parallel components of this forcing term by substituting the velocity components of pump KAWs as given in equations (4), (6), (7) and (9) and averaging the Lorentz and the convective terms over the pump KAW time period of $2\pi/\omega$ (P. Shukla & Stenflo, 2000b).

$$\begin{aligned} F_z &= F_{ez} + F_{iz} \\ &\simeq -\frac{e^2}{4\omega^2 m_e}\frac{\partial}{\partial z}|\delta E_z|^2 + \frac{e^2}{4m_i\left(\omega_{ci}^2 - \omega^2\right)}\frac{\partial}{\partial z}|\delta E_x|^2 \\ &+ \frac{e^2}{4m_i\left(\omega_{ci}^2 - \omega^2\right)}\frac{\partial}{\partial z}|\delta E_y|^2. \end{aligned} \tag{45}$$

Now, let us evaluate the expressions for the perturbed electric fields to be substituted in equation (45). From equation (23), we get

$$\delta E_z = \frac{c\omega k_{0x}}{\omega_{pe}^2}\delta B_y. \tag{46}$$

From equation (26) and (27) we get,

$$\delta E_y = \frac{\beta}{2}\left(ik_{0z}\right)\frac{c\omega_{ce}}{\omega_{pe}^2}\delta B_y. \tag{47}$$

Using equations (26) and (27) in equation (25), we get

$$\delta E_x = \frac{\lambda_e k_{0z}\omega_{ce}\omega_{ci}}{\omega\omega_{pe}}\left[\left(1 - \frac{\omega^2}{\omega_{ci}^2}\right) - \frac{\beta}{2}\right]\delta B_y. \tag{48}$$

Substituting equation (45) into equation (44) along with equations (46), (47) and (48) and taking the magnetic field perturbations (δB_y) as a plane wave modulated by a slowly

varying envelope $\delta\tilde{B}_y$ as previously defined in equation (33), we get

$$\left(\frac{\partial^2}{\partial t^2} - c_s^2\frac{\partial^2}{\partial z^2}\right)\delta n = -\frac{e^2 n_0}{4m_e m_i}\frac{c^2 k_{0x}^2}{\omega_{pe}^4}\left[\frac{\left[\left(1-\omega^2/\omega_{ci}^2\right)-\beta\right]^2}{\lambda_e^2 k_{0x}^2\left(1-\omega^2/\omega_{ci}^2\right)} - \frac{m_i}{m_e}\frac{k_{0z}^2}{k_{0x}^2}\frac{\beta^2}{\left(1-\omega^2/\omega_{ci}^2\right)}\right]\frac{\partial^2}{\partial z^2}|\delta\tilde{B}_y|^2. \tag{49}$$

Normalizing the pump KAW dynamical equation (34) and the ion acoustic wave equation (49), we get the following set of equations

$$i\frac{\partial\left(\delta B_y\right)}{\partial t} + i\frac{\partial\left(\delta B_y\right)}{\partial x} + c_1\frac{\partial^2\left(\delta B_y\right)}{\partial x^2} + c_2\frac{\partial^2\left(\delta B_y\right)}{\partial z^2} + i\frac{\partial\left(\delta B_y\right)}{\partial z} + c_3\frac{\partial^2\left(\delta B_y\right)}{\partial t\partial x} - ic_4\frac{\partial^3\left(\delta B_y\right)}{\partial t\partial x^2} - ic_5\frac{\partial^3\left(\delta B_y\right)}{\partial x^2\partial z} - c_6\frac{\partial^4\left(\delta B_y\right)}{\partial x^2\partial z^2} - ic_7\frac{\partial^3\left(\delta B_y\right)}{\partial x\partial z^2} + c_8\frac{\partial^2\left(\delta B_y\right)}{\partial x\partial z} + (1-\omega^2/\omega_{ci}^2)(\delta n)(\delta B_y) = 0 \tag{50}$$

and

$$\frac{\partial^2\left(\delta n\right)}{\partial t^2} - c_9\frac{\partial^2\left(\delta n\right)}{\partial z^2} = -\frac{\partial^2\left(|\delta B_y|^2\right)}{\partial z^2}. \tag{51}$$

Here, we have denoted $\delta\tilde{B}_y$ as δB_y by removing the mark $\sim$ placed on top of δB_y for the sake of writing.

The dimensionless parameters appeared above are: $c_1 = \frac{v_{te}^2\lambda_e^2 k_{0z}^2 - \lambda_e^2\omega^2}{v_A^2 k_{0z}^2 x_n^2}$, $c_2 = \frac{v_{te}^2\lambda_e^2 k_{0x}^2 + cB_0\beta\omega_{ci}/8\pi n_0 e + v_A^2(1-\omega^2/\omega_{ci}^2)}{v_A^2 k_{0z}^2 z_n^2}$, $c_3 = \frac{4\lambda_e^2\omega k_{0x}}{v_A^2 k_{0z}^2 t_n x_n}$, $c_4 = \frac{2\lambda_e^2\omega}{v_A^2 k_{0z}^2 t_n x_n^2}$, $c_5 = \frac{2k_{0z}v_{te}\lambda_e^2}{v_A^2 k_{0z}^2 x_n^2 z_n}$, $c_6 = \frac{v_{te}^2\lambda_e^2}{v_A^2 k_{0z}^2 x_n^2 z_n^2}$, $c_7 = \frac{2k_{0x}v_{te}^2\lambda_e^2}{v_A^2 k_{0z}^2 x_n z_n^2}$, $c_8 = \frac{4k_{0x}k_{0z}v_{te}^2\lambda_e^2}{v_A^2 k_{0z}^2 x_n z_n}$, and $c_9 = \frac{c_s^2 t_n^2}{z_n^2}$.

The normalising parameters are: $t_n = \frac{2\omega\left(1+\lambda_e^2 k_{0x}^2\right)}{v_A^2 k_{0z}^2}$, $x_n = \frac{2\left(v_{te}^2\lambda_e^2 k_{0z}^2 k_{0x} - k_{0x}\lambda_e^2\omega^2\right)}{v_A^2 k_{0z}^2}$, $z_n = \frac{2k_{0z}\left[v_{te}^2\lambda_e^2 k_{0x}^2 + \frac{cB_0\beta\omega_{ci}}{8\pi n_0 e} + v_A^2\left(1-\frac{\omega^2}{\omega_{ci}^2}\right)\right]}{v_A^2 k_{0z}^2}$, $n_n = n_0$ and

$B_n = \left(\frac{z_n^2 n_n m_i\omega_{pe}^4}{Mt_n^2\omega^2 c^2 k_{0x}^2}\right)^{1/2}$, where M is a dimensionless parameter given by

$M = \frac{n_0 e^2}{4m_e\omega^2}\left[\frac{\left(1-\omega^2/\omega_{ci}^2-\beta\right)^2}{\lambda_e^2 k_{0x}^2\left(1-\omega^2/\omega_{ci}^2\right)} - \frac{m_i}{m_e}\frac{k_{0z}^2}{k_{0x}^2}\frac{\beta^2}{1-\omega^2/\omega_{ci}^2}\right]$.

3 Numerical Simulation

The equations (50) and (51) constitute modified ZSEs describing the nonlinear coupling between pump KAWs (dispersive) and ion acoustic waves (approximately non-dispersive). In the adiabatic limit, this system of equations becomes modified Nonlinear Schrodinger Equation (NLSE) with the substitution of density perturbation as $\delta n \propto |\delta B_y|^2$. We performed a numerical simulation of the modified ZSEs using the pseudo-spectral method where the spatial derivatives can be calculated using orthogonal functions such as Fourier integrals, Chebyshev polynomials etc. In our simulation, we used the Fourier integrals evaluated using Fast Fourier Transform (FFT), thereby converting the space derivatives into the wavenumber domain by multiplication of the spectrum with ik where k is the wavenumber. The inverse Fourier Transform gives the exact space derivative up to the Nyquist frequency. The spatial integration was carried out at $2^7 \times 2^7$grid points with a periodic domain of dimensions $L_x = \frac{2\pi}{\alpha_x}$ and $L_z = \frac{2\pi}{\alpha_z}$, where α_x and α_z represent the perturbation wavenumbers in the x and z directions normalized by x_n^{-1} and z_n^{-1} respectively. The temporal first derivative was evaluated in Fourier space using Newton's forward difference with a step size of $dt = 5 \times 10^{-5}$ and then the leap-frog time step method and predictor-corrector method. Such difference approximations to differential

equations are accurate when the wavenumbers are low enough. As the wavenumbers increase, the linear terms dominate the nonlinear terms in the differential equation, hence reducing the accuracy. To circumvent this, we modified the linear terms in the leap-frog step using the ideas of Fornberg and Withham (Fornberg & Whitham, 1978). On the other hand, if we calculate the nonlinear terms directly in Fourier space it leads to the convolution involving N^2 operations for quadratic nonlinearity, where N is the number of grid points. In case of higher nonlinearity, the situation gets even worse involving more operations. To overcome this problem, instead of evaluating the nonlinear terms in Fourier space directly, we transformed the involved variables back to real space and evaluated the nonlinearity in real space and then in Fourier space. With this procedure the number of operations involved in quadratic nonlinearity is reduced to $N \log N$, yielding fast computational speed.

We first developed an algorithm to solve 2D-cubic NLSE and compared the results with other available results. The NLSE is an important and well-known model of nonlinear phenomena in fluids and plasmas. To test the numerical code, we set the benchmark of the algorithm by calculating the conservation of the plasmon number given by

$$P = \frac{1}{L_x}\frac{1}{L_z}\int_0^{L_x}\int_0^{L_z} |\delta B_y|^2 dxdz = \int_{-\infty}^{\infty}\int_{-\infty}^{\infty} |\delta B_{yk}|^2 dk_x dk_z = \sum_k |\delta B_{yk}|^2,$$

which is conserved up to the accuracy of 10^{-6}. The same code was modified for the modified ZSEs of our problem which is nonintegrable. On the other hand, the discrete Fourier transform of a periodic function introduces the so called aliasing error at each time step simulated with finite grid resolution when the nonlinear interactions are not fully resolved in the fixed computational grids. In the quadratic nonlinear term, the aliasing errors occur when the addition of the wave numbers (k_1+k_2) exceeds the Nyquist sampling criterion, i.e., $(k_1 + k_2) > N$ where k_1, $k_2 \in \left[-\frac{N}{2}+1, \frac{N}{2}\right]$, N is the number of equidistant discrete points in spatial directions. In our simulation, we used a phase shift dealiasing scheme which is described here briefly for the sake of completeness. In evaluating the nonlinear term $(f_j g_j)$ of variables f and g at grid points $j = 0, 1, ..., (N-1)$, the dealiasing operation is performed by taking the Fourier transform at the shifted grid points. The variables f and g at real space are represented as (Yin et al., 2005; Sinhababu & Ayyalasomayajula, 2021)

$$f_j^s = \sum_{|k|\leq \frac{N}{2}} \hat{f} e^{i(x_j+\Delta)}, \tag{52}$$

$$g_j^s = \sum_{|k|\leq \frac{N}{2}} \hat{g} e^{i(x_j+\Delta)}, \tag{53}$$

where x_j is the collocation points and the superscript s denotes the variables in the shifted grids. The next step is the multiplication of these variables in the shifted grid as

$$\mathcal{NL}_j^s = f_j^s . g_j^s. \tag{54}$$

Fourier transform of the nonlinear terms at the shifted grids is obtained as

$$\widehat{\mathcal{NL}^s} = \frac{1}{N}\sum_{j=0}^{N-1} \mathcal{NL}_j^s e^{-i(x_j+\Delta)}. \tag{55}$$

It can be expressed as (Patterson Jr & Orszag, 1971; Canuto et al., 2007; Kopriva, 2009)

$$\widehat{\mathcal{NL}^s} = \sum_{p+q=k} \hat{f}_p \hat{g}_q + e^{\pm iN\Delta}\left(\sum_{p+q=k\pm N} \hat{f}_p \hat{g}_q\right). \tag{56}$$

Taking $\Delta = \pi/N$, the nonlinear terms free from aliasing error are obtained as (Canuto et al., 2007)

$$\widehat{\mathcal{NL}} = \frac{1}{2}\left(\widehat{\mathcal{NL}^s} + \sum_{p+q=k} \hat{f}_p \hat{g}_q\right). \tag{57}$$

Since the linear evolution in the differential equation is exactly integrable, a plane wave solution is a possible solution. We used a uniform plane pump KAW of fixed amplitudes superimposed by a sinusoidal periodic perturbation as the initial condition of the simulation as

$$\delta B_y(x, z, t = 0) = \delta B_{y0}[1 + \epsilon \cos(\alpha_x x)] \times [1 + \epsilon \cos(\alpha_z z)], \tag{58}$$

where ϵ represents the magnitude of the perturbation and δB_{y0} is the amplitude of the pump KAW. Although the magnetic waves in astrophysical plasmas are more complicated, they can be represented as the sum of the sinusoidal wave components.

The initial condition of the density perturbation was taken as

$$\delta n = |\delta B_y|^2. \tag{59}$$

The modified ZSEs (50) and (51) were simulated for two different regions based on the plasma β values (a) the Earth's radiation belt ($\beta < 1$) and (b) near-Sun streamer belt solar wind ($\beta > 1$) at distance of $\approx$ 0.13 AU to 0.25 AU from the surface of the Sun. In the simulation, we used $\delta B_{y0} = 1$, $\epsilon = 0.1$, and $\alpha_x = \alpha_y = 0.01$. The plasma parameters chosen for the radiation belt are (Cattell et al., 2008; Goyal et al., 2018): $B_0 \approx 5.0\times10^{-3}$ G, $n_0 \approx 5.0$ cm^{-3}, $T_e \approx 6.0\times10^6$ K and $T_i \approx 1.1\times10^8$ K. Employing these values, the other parameters are calculated as $\beta \approx 4.16 \times 10^{-3}$, $w_{ce} \approx 8.8 \times 10^4$ s^{-1}, $w_{ci} \approx 47.9$ s^{-1}, $\omega_{pe} \approx 1.261 \times 10^5$ s^{-1} and $\lambda_e \approx 2.37 \times 10^5$ cm. We used $\omega/\omega_{ci} = 0.02$ for a finite frequency and $k_{0x}\lambda_e = 0.2$. Accordingly, we calculated other parameters and the normalizing parameters corresponding to the radiation belt, which are tabulated in the table 1.

The plasma parameters chosen for the near-Sun streamer belt solar wind were taken from the fourth orbit of the PSP when it reaches around $28 - 54$ solar radii (C. Chen et al., 2021; Liewer et al., 2023) are: $B_0 \approx 5.0 \times 10^{-4}$ G, $n_0 \approx 10^3$ cm^{-3} and $T_e \approx 5.0\times10^5$ K. Employing these values, the other parameters are calculated as $\beta \approx 6.94$, $w_{ce} \approx 8.79 \times 10^3$ s^{-1}, $w_{ci} \approx 4.79$ s^{-1}, $\omega_{pe} \approx 1.78 \times 10^6$ s^{-1} and $\lambda_e \approx 1.68 \times 10^4$ cm. We used $\omega/\omega_{ci} = 0.02$ for a finite frequency and $k_{0x}\lambda_e = 0.2$. Accordingly, we calculated other parameters and the normalizing parameters corresponding to the near-Sun streamer belt solar wind, which are tabulated in the table 1.

We analyze here the numerical results of the modified ZSEs applicable to the Earth's radiation belt. First, the magnetic field intensity profiles of KAWs in the form of generation of filaments are shown in figure 1 at six different instants of normalized times ($t = 0.5, 13, 18, 44, 75,$ and 95). It is evident from the figure that the magnetic field intensities are localized in space with periodic patterns initially and with the evolution of time, it changes to quasiperiodic and chaotic structures. The nonlinear ponderomotive force exerted by the pump KAW induces the background density variations, leading to changes in the phase velocity of KAWs. The changes in the phase velocity result in the spatial localization of KAWs in the $x-z$ plane. In astrophysical plasma, the process of magnetic coherent (localized) structures generation of waves is the same as that of laser beam filamentation in laboratory plasma. When a high-power laser beam propagates through plasma, the associated ponderomotive force modifies the plasma density, thereby varying the refractive index of the medium. In this way, the medium acts as a converging lens, producing a focused laser beam. In a similar way, when KAWs propagate through astrophysical plasma, the parallel ponderomotive force acting on the plasma will produce variations in the density resulting in varying phase velocity. This will generate spatial localization of KAWs having coherent structures. As time evolves, the perturbations associated with the pump KAWs take the magnetic energy leading to the collapse of the magnetic coherent structures. However, due to the nonlinear interactions of magnetic field and density, these collapsed structures try to regroup as time advances. These structures become more intense and chaotic with the advancement of time, reaching the high-

est amplitude as well as more chaotic distribution at $t = 95$ shown in figure 1(f). Beyond this time, we cannot see any significant changes in the magnetic field intensity profiles as the modulational instability saturates. It means at $t = 95$, the system reaches a quasi steady state. Although the evolution of the magnetic field coherent structures is dependent on the initial conditions and the nonlinearities involved, once the quasi steady state is reached, the system is no more dependent on these conditions. The transverse scale size of the localized magnetic filaments at $t = 0.5, 13$ and 18, as shown in figure 1(a)-(c) are of the order of ion gyroradius or ion inertial length which is the energy injection scale, whereas it is electron gyroradius or electron inertial length for $t = 44, 78$ and 95 as shown in figure 1(d)-(f) which is the energy dissipation scale. In the collapse magnetic structures or density gradient regions, large parallel electric fields are generated that can accelerate the electrons along the direction of the background magnetic field (Génot et al., 2000; Tsiklauri, 2012). At sufficiently large fluctuations in the parallel fields and the current densities, the electrons can be trapped in between the wave packets (filaments) (Gershman et al., 2017). As the waves propagate, their kinetic energy is converted to particle energy, the process that can be considered as a magnetic analog of Landau damping. If the size of the wave packets is smaller than the ion acoustic gyroradius ρ_i, the ion motion decouples from the electron motion. From the fluctuating magnetic intensity profiles, we found that in the early stages of magnetic field evolution, the size of the transverse filaments is of the order of the ion gyroradius ($\approx 6\rho_i \approx 10^4$ km) at half of the intensity peak as also observed by Lion et al. (2016) and Passot et al. (2014). As the system evolves, these filamentary structures undergo a transverse collapse, significantly reducing their size to less than the characteristic length scale ρ_i. When the size of the filaments reaches the kinetic scale comparable to the short perpendicular wavelength of KAWs, the energization of plasma particles can happen through wave-particle energy exchange.

Figure 2 depicts density fluctuations along $z-$direction at different times applicable for the Earth's radiation belt corresponding to figure 1. Before the turbulent state, density cavitons (humps) are formed [figure 2(a)-(d)]. Because of the ponderomotive force, the magnetic field is trapped in the regions of density cavities producing magnetic coherent structures. However, as the perturbation associated with the pump KAW takes the magnetic energy, the magnetic coherent structures tend to collapse. Due to the nonlinear interactions of magnetic field and density, these collapsed structures try to regroup as time advances. Therefore, we can see only density cavitons (humps) and no density depletions till $t = 44$ (figure 2(d)) before the turbulent state was set. In figure 2(e) we can see small density depletions at $z \approx \pm 300$ where the system starts to be in a chaotic state. In figure 2(f) when the system reaches the quasi steady turbulent state, many density humps and depletions are observed. One can study the phenomenon of turbulence by examining the cascading of energy and the process of density cavitation through ZSEs as suggested by Doolen et al. (1985). They suggested that Langmuir waves are localized when the wave packets are trapped in density cavities. Also, Sharma et al. (1996) studied the Langmuir turbulence by energy cascades and cavitation process.

It is worth mentioning here that ion acoustic waves generate solitons with density humps in electron-ion plasma (Davidson, 2012). In electron-positron-ion plasma, the amplitudes of the ion acoustic waves will be reduced, producing density dips depending on the strength of the positron concentrations (Popel et al., 1995). A similar method of producing density humps and dips was also reported in the case of KAWs. Many decades ago, Hasegawa and Mima (1976) predicted that density humps would be produced when KAWs propagate in electron-ion plasma at sub-Alfvénic regime. In the super-Alfvénic regime, the KAWs produce density dips in electron-positron-ion plasma(Saleem & Mahmood, 2003). Similar results were also obtained by studying the nonlinear KAWs in dusty plasma (Yinhua et al., 2000) and quantum magnetoplasma (Sadiq et al., 2018b) . However, all these studies did not consider the coupling of ion acoustic waves with KAWs when the effect of ion inertia in parallel motion is taken into account.

In order to analyse the evolution of the magnetic field in Fourier modes, we plotted $|\delta B_{yk}|$ as a function of t (figure 3) across three distinct modes: Mode A ($k_x = 1$, $k_z = 0$), Mode B ($k_x = 2$, $k_z = 0$) and Mode C ($k_x = 3$, $k_z = 0$) where k_x and k_z are wavenumbers of KAWs generated by the interaction of pump KAWs (having wavenumbers k_{0x} and k_{0z}) and ion acoustic waves propagating in an inhomogeneous plasma medium. It is observed from the figure that the major participants in the energy sharing process are mostly confined to low wavenumber modes. Mode A has the maximum share of energy at initial time, but it decays with time sharing its energy with other higher modes B and C showing an oscillatory evolution.

To study the distribution of magnetic energy across various wavenumbers, we plotted $|\delta B_{yk}|^2$ against $k_x(k_\perp)$ represented by figure 4. At $t = 0.5$, only a single wave mode exists, but higher harmonics are generated at later times. Initially, magnetic energy is concentrated in low wavenumber modes, but it becomes distributed across higher wavenumber modes as time progresses. Further, to understand more about the turbulent behaviour of the magnetic field in radiation belt plasma, we have studied the fluctuating magnetic field spectrum $|\delta B_{yk}|^2$ versus $k_\perp$ (averaged over $k_\parallel$) plotted at $t = 95$ (figure 5) when the turbulence has reached the quasi steady state. It is evident that for scales larger than ion inertial length ($k_\perp \rho_i < 1$) known as inertial range created by energy conserving spectral cascade (Smith et al., 2006), the fluctuating magnetic spectrum approaches the Kolmogorov scaling with a spectral index of $-5/3$ (i.e., $|\delta B_{yk}|^2 \propto k_\perp^{-5/3}$). In the inertial regime, fluid dynamics can still be used to study the interactions between fluctuations. In many solar and magnetospheric plasmas, the Kolmogorov spectral index of $-5/3$ (Borovsky, 2012; Shaikh & Zank, 2009; Xu et al., 2023) as well as the Iroshnikov-Kraichnan spectral index of $-3/2$ (Smith et al., 2006; Podesta, 2011; Zhao, Zank, Adhikari, et al., 2022) have been reported. Beyond this range, steepening in the magnetic field power spectrum occurs as such individual particle effects and thermal heating take over (Leamon et al., 1998; Smith et al., 2006; Alexandrova et al., 2008; Lion et al., 2016) which is regarded as dissipation range. From the power spectrum (figure 5) we can see that the first spectral break appeared at $k_\perp \rho_i \approx 0.76$ which corresponds to the transition from the inertial range (ion scale) to the kinetic range (electron scale). For $k_\perp \rho_i > 0.76$ the spectral index is much steeper which is ~ -3. By analyzing Van Allen Probes observations, Moya et al. (2015) reported magnetic frequency power spectral indices of -1.1 to -1.7 for frequency $\gtrsim 2\ Hz$ (inertial range) and -4 to -5 for frequency $\lesssim 2\ Hz$ (sub kinetic scale) that are consistent with weak KAW turbulence. Some authors (Markovskii et al., 2006; Bruno & Trenchi, 2014; Lion et al., 2016) have also reported varying spectral indices between -1 and-4, depending on turbulent fluctuations. The steepening of the spectral index is an indication that the transfer of energy from a larger scale (lower frequency) to a smaller scale (higher frequency) happens. This may be considered as one reason to accelerate the plasma particles, thereby increasing the plasma temperature. As the plasma particles take away some of the energy of the fluctuations, it leads to the energization of the plasma which could be the main reason for the steeper spectrum. The physical process involving the transition from inertial to dissipation range at ion-kinetic scales is still an ongoing inquiry (Bowen et al., 2020; Matteini et al., 2020; Terres & Li, 2022).

We have also performed the numerical simulation of the modified ZSEs for $\beta > 1$, applicable for the parameters in the near-Sun streamer belt solar wind. The essential plasma and simulation parameters are given in the table 1. The same trends of magnetic filament formation, regrouping and collapsing at later times happened. Since, it has almost the same characteristics as that of the radiation belt corresponding to $\beta < 1$, instead of showing all the graphical results and analyzing it in detail, we are showing here the fluctuating magnetic field power spectrum plotted at $t = 76$ when the quasi-steady state is reached (figure 6) and reporting few basic differences from the two regions. In the case of near-Sun streamer belt solar wind, there is an increase in total magnetic power fluctuations and spectral break wavenumber ($k_\perp \rho_i \approx 1$) with a more steep spec-

tral index of -4 in the dissipation range (figure 6) in comparison to the -3 of the radiation belt region. In order to understand the spectral properties of the magnetic field fluctuations in the inner heliosphere, many researchers (Šafránková et al., 2023; Lotz et al., 2023), carried out a statistical study on PSP and Solar Orbiter data at various distances from the Sun. Šafránková et al. (2023) found the inertial range spectral index of $-3/2$ at the closest approach (0.12 AU) to the Sun, then becoming steeper as it moves away, reaching $-5/3$ at around 0.4 AU. A similar trend of transition from $-3/2$ to $-5/3$ when the solar wind passes from 0.17 AU to 0.60 AU was also investigated by C. H. K. Chen et al. (2020). By analysing the PSP magnetic field observations Zhao, Zank, Telloni, et al. (2022) reported a $-5/3$ spectral index in the inertial region. In the dissipation range, it was -4.8 at the closest approach to the Sun then becoming more flat as it moves away, approaching it to ≈ -3 at around 0.4 AU (Šafránková et al., 2023). From 0.4 AU to 1 AU, the spectral indices remain approximately constant ($-5/3$ at inertial and ≈ -3 at dissipation range). Lotz et al. (2023) found the inertial range spectral index varying between -1.45 to -1.65 and the dissipation range spectral index varying between -4 at 0.1 AU to -3 at 0.7 AU. The steepening of the spectral index as the PSP moves towards the Sun can be attributed to the enhanced power of the turbulence with decreasing radial distance from the Sun (Smith et al., 2006; Bruno & Trenchi, 2014; Huang et al., 2021). The increase of magnetic power fluctuations and spectral break wavenumber towards the Sun is expected (Lotz et al., 2023).

Many authors (Velli, 2003; Wu et al., 2016; Malara et al., 2019; Nättilä & Beloborodov, 2022) proposed that dissipation of Alfvén waves leading to turbulent energy cascade in high wavenumbers may be responsible for heating the astrophysical plasmas. They calculated the energy flux density in the coronal loops and found it to be consistent with the observational results. However, the physical mechanism behind this turbulent energy cascade has not been satisfactorily explained till now. The transverse collapse of KAWs via magnetic filaments may be considered as one of the reasons to explain Kolmogorov turbulence and dissipation range heating. To sufficiently heat the solar corona by small-scale bursts such as solar flares, Hudson (1991) and others (Tu & Marsch, 2001; Simnett, 2005) found that the energy spectral index has to be much steeper than -2. Such kind of steep spectral index has also been pointed out in the quite-Sun and active regions by analyzing the observational data from many spacecraft such as *Yohkoh* with SXT, *SOHO* and *TRACE* (Phillips, 2000; Aschwanden & Parnell, 2002; Domingo, 2002). It should be mentioned here that our present KAW model is valid for $k_\perp \rho_i \lesssim 1$ because of the low frequency condition $\omega < \omega_{ci}$. For $k_\perp \rho_i \gg 1$, the waves at electron scales lead to Landau damping via wave particle interactions (Gary & Nishimura, 2004; Sahraoui et al., 2009; Bian et al., 2010). In this region, whistler mode $\omega > \omega_{ci}$ may be more relevant. However, the origin of fluctuating turbulent spectra at small scales has not been properly resolved despite many studies suggesting it due to different wave modes such as whistler waves, ion cyclotron waves, Alfvén cyclotron waves, KAWs, magnetosonic waves, ion acoustic waves or interactions among these waves (Dwivedi et al., 2012; Boldyrev et al., 2013; L. Chen et al., 2013; López et al., 2017). Therefore, our present model of KAW dynamics coupled with density perturbations generated by ion acoustic waves due to the parallel ponderomotive force leading to the transverse collapse of the magnetic coherent structures may be one of the candidates to explain the physical process of turbulence and the particle heating in various astrophysical plasmas.

4 Particle Heating

When turbulent KAW amplitudes exceed a certain threshold, the proton motion perpendicular to the background magnetic field $\mathbf{B_0}$ becomes chaotic (Johnson & Cheng, 2001; C. Chaston et al., 2004; Fiksel et al., 2009). The protons then interact stochastically with the time-varying electrostatic potential and proton energy can be reasonably approximated by a random walk. If a single proton performs a random walk in en-

ergy, it can gain or lose energy with the same probability during a time Δt. However, if the number of thermal protons (initially having isotropic Maxwellian distribution in velocity) is large, then they will gain more energy leading to stochastic proton heating (Hoppock et al., 2018). Using phenomenological arguments, the proton heating rates for low β plasma ($\beta \ll 1$) and high β plasma ($\beta \sim 1-30$) were calculated at $k_\perp \rho_i \sim 1$ by Chandran et al. (2010) and Hoppock et al. (2018) respectively. The repetitive interactions of charged particles with the collapsed magnetic structures can heat the particles via the second-order Fermi acceleration mechanism as explained by Ichimaru and Yakimenko (1973), Fuchs et al. (1985) and Rozmus et al. (1987). The continuous interactions of particles with wave packets can be modelled within the Quasi-Linear Theory using the Fokker–Planck diffusion equation (Fuchs et al., 1985; Rozmus et al., 1987) given by

$$\frac{\partial f}{\partial t} = \frac{\partial}{\partial v}\left(D(v)\frac{\partial f}{\partial v}\right), \tag{60}$$

where $D(v)$ and $f(t, v)$ are the diffusion coefficient and velocity distribution function respectively and the diffusion coefficient (Fuchs et al., 1985; Rozmus et al., 1987) is given as

$$D(v) = \frac{1}{4}\left(\frac{Q}{m_i}\right)^2 l_A \int dk |\delta E_k|^2 \delta(\omega - kv) = \frac{1}{4}\left(\frac{Q}{m_i}\right)^2 l_A \frac{1}{|v|}|\delta E_k|^2_{k=\omega/v}. \tag{61}$$

Here, Q is the ionic charge and l_A is the periodicity length. From equation (30) we can find out the parallel component of the perturbed electric field in Fourier space as

$$\delta E_{zk} = \left[\frac{\lambda_e^2 \omega k_{0x}}{c} - \frac{v_{te}^2 \lambda_e^2 k_{0x} k_{0z}^2}{c\omega}\right] \delta B_{yk}. \tag{62}$$

The value of $|\delta E_{zk}|$ for continuously changing k ($k_{\min} \leq k \leq k_{\max}$) where $k_{\max}$ and $k_{\min}$ denote the wavenumbers at the boundaries of the fluctuating field region can be determined by examining the overall shape of the Fourier spectrum of the magnetic field by using the approximation $|\delta E_{zk}| = |\delta E_{zk_{\min}}| \, [|k_{\min}/k|]^{\eta/2}$. Here, η represents the spectral index of the power spectrum.

In normalised form equation (60) can be written as

$$\frac{\partial f}{\partial \tau} = \frac{\partial}{\partial u}\left(D(u)\frac{\partial f}{\partial u}\right), \tag{63}$$

where the velocity is normalized by the thermal velocity of ions, $v_{thi} = \sqrt{k_B T_i/m_i}$, $D(v)$ by $D(v_0)$, and $f(t, v)$ by $f(0, 0)$. We used the scale time $\tau = (v_{thi})^2/D(v_0)$, where $D(v_0)$ is given by

$$D(v_0) = \frac{1}{4}\left(\frac{Q}{m_i}\right)^2 l_A \frac{|\delta E_{k_{min}}|^2}{v_{k_{min}}}. \tag{64}$$

How the particle distribution function evolves in the presence of stochastic heating has remained unanswered (Chandran et al., 2010; Hoppock et al., 2018). However, we can neglect the time dependence of the distribution function when it reaches a constant value if the observation time (t_{obs}) is much greater than the characteristic time (t_d) taken to generate the ponderomotive nonlinearity to set up which is of the order of r_0/c_s, where r_0 is the transverse scale size of the filament of KAWs and c_s is the ion sound speed. Under this assumption, the particle distribution function is of the form of $f(v) \propto v^{2+\eta}$ (Sharma & Kumar, 2010) where η has the negative spectral slope. In our case $\eta \approx -3$ and -4 in the dissipation range of the Earth's radiation belt and near-Sun streamer belt solar wind regions, that gives $f(v) \propto v^{-1}$ and $f(v) \propto v^{-2}$ respectively. The distribution function is sensitive to the spectral index that leads to the formation of thermal tail of the energetic particles in the astrophysical plasma. To solve equation (63) numerically, we used a Maxwellian distribution function as the initial condition and plotted the distribution function with velocity at different scaled times τ ($\tau = 0$ and $\tau = 30$) and spectral indices ($-5/3$ and -3) as shown in figure 7. We have chosen $\tau = 30$ in such a way

that at this scaled time $t_{obs} \gg t_d$, the wave spectrum reaches a quasistationary state. From figure 7, it is observed that the fluctuating fields accelerate the particles, hence populating the superthermal tail. The extension of the superthermal tail is dependent on the fluctuating fields and the spectral indices.

5 Conclusion

We have numerically analyzed the modified ZSEs governing the coupled dynamics of KAWs and ion acoustic waves applicable to low $\beta < 1$, the Earth's radiation belt plasma and high $\beta > 1$, near-Sun streamer belt solar wind plasma. The simulations demonstrated the generations of magnetic field filaments or coherent structures due to the density variations produced by the ponderomotive force exerted by the pump KAWs. These magnetic filaments exhibit an initial periodic pattern that evolves into quasi-periodic and chaotic structures over time. The analysis of the magnetic field power spectra reveals a Kolmogorov-like inertial range with a spectral index of $-5/3$ for scales larger than the ion inertial length, followed by a steeper dissipation range with spectral indices of approximately -3 for the radiation belt plasma and -4 for the near-Sun streamer belt solar wind plasma. In the case of near-Sun streamer belt solar wind, there is an increase in total magnetic power fluctuations and spectral break wavenumber $k_\perp \rho_i \approx 1$, in comparison to spectral break wavenumber $k_\perp \rho_i \approx 0.76$ in the radiation belt region. The steepening of the spectrum in the dissipation range indicates the transfer of energy from larger to smaller scales, potentially leading to particle energization and heating. Using the quasilinear theory represented by the Fokker–Planck equation and correlating it with the magnetic fluctuation power spectra, we obtained the particle distribution function. We found the extension of the superthermal tail indicating the particle energization that depends on the fluctuating fields and the spectral indices. We studied the following two phenomena independently: (i) generation of turbulence and (ii) heating produced by the wave particle interaction due to turbulence. However, it has to be studied self consistently by accounting for the energy gained by the particles in terms of damping of the pump KAW energy. It can be achieved by including a Landau damping term to the pump KAW dynamics as the viscous term is included in the hydrodynamic fluid equation. Moreover, for plasma $\beta > 1$, the kinetic effects of Landau damping play a vital role in the wave particle interaction. Although Landau damping is a purely kinetic phenomenon, there is a way to consider it within the fluid theory as suggested for the first time by Dangelo et al. (1979) to describe its effects on the fast solar wind streams. According to this model a dissipative term of the shape of $\mu\nabla^2 v$, where μ is the damping coefficient, has to be included in the momentum equation. The damping coefficient can be chosen in such a way that it matches the experimentally verified features of kinetic Landau damping. This is the limitation of the present work which we are planning to incorporate in our future work.

6 Data Availability Statement

The Fortran code to solve the modified ZSEs equations (50) and (51) is available in Github: `https://github.com/hemam12/Pseudo-Spectral-Method` and preserved in a repository in Zenodo along with the output data files generated after compiling the code and the MATLAB script files used to plot the figures: `https://doi.org/10.5281/zenodo.11096895`.

Acknowledgments

The authors are thankful to Sikkim University for providing the centralised High Performance Computational facility at the Brahmagupta Lab. Authors Mani K Chettri and Vivek Shrivastav are grateful to the University Grants Commission, India for providing Non-NET fellowship.

References

Alazraki, G., & Couturier, P. (1971). Solar wind acceleration caused by the gradient of alfven wave pressure. *Astronomy and Astrophysics*, *13*, 380.

Alexandrova, O., Carbone, V., Veltri, P., & Sorriso-Valvo, L. (2008). Small-scale energy cascade of the solar wind turbulence. *The Astrophysical Journal*, *674*(2), 1153.

Alexandrova, O., Chen, C. H. K., Sorriso-Valvo, L., Horbury, T. S., & Bale, S. D. (2013). Solar wind turbulence and the role of ion instabilities. *Space Science Reviews*, *178*(2-4), 101-139.

Alexandrova, O., Saur, J., Lacombe, C., Mangeney, A., Mitchell, J., Schwartz, S. J., & Robert, P. (2009). Universality of solar-wind turbulent spectrum from mhd to electron scales. *Physical Review Letters*, *103*(16), 165003.

Aschwanden, M. J., & Parnell, C. E. (2002). Nanoflare statistics from first principles: fractal geometry and temperature synthesis. *The Astrophysical Journal*, *572*(2), 1048.

Bale, S. D., Balikhin, M. A., Horbury, T. S., Krasnoselskikh, V. V., Kucharek, H., Möbius, E., et al. (2005). Quasi-perpendicular shock structure and processes. *Space Science Reviews*, *118*, 161–203.

Barik, K. C., Singh, S. V., & Lakhina, G. S. (2021). Kinetic alfvén waves in space plasma environment with k-electrons. *The Astrophysical Journal*, *919*(2), 71.

Bavassano, B., Pietropaolo, E., & Bruno, R. (2004). Compressive fluctuations in high-latitude solar wind. In *Annales geophysicae* (Vol. 22, p. 689-696).

Bian, N., Kontar, E., & Brown, J. (2010). Parallel electric field generation by alfvén wave turbulence. *Astronomy & Astrophysics*, *519*, A114.

Boldyrev, S., Horaites, K., Xia, Q., & Perez, J. C. (2013). Toward a theory of astrophysical plasma turbulence at subproton scales. *The Astrophysical Journal*, *777*(1), 41.

Borovsky, J. E. (2012). The velocity and magnetic field fluctuations of the solar wind at 1 au: Statistical analysis of fourier spectra and correlations with plasma properties. *Journal of Geophysical Research: Space Physics*, *117*(A5).

Bowen, T. A., Mallet, A., Bale, S. D., Bonnell, J., Case, A. W., Chandran, B. D., ... others (2020). Constraining ion-scale heating and spectral energy transfer in observations of plasma turbulence. *Physical review letters*, *125*(2), 025102.

Bruno, R., & Trenchi, L. (2014). Radial dependence of the frequency break between fluid and kinetic scales in the solar wind fluctuations. *The Astrophysical Journal Letters*, *787*(2), L24.

Burlaga, L. F., Scudder, J. D., Klein, L. W., & Isenberg, P. A. (1990). Pressure-balanced structures between 1 au and 24 au and their implications for solar wind electrons and interstellar pickup ions. *Journal of Geophysical Research: Space Physics*, *95*(A3), 2229-2239.

Canuto, C., Hussaini, M. Y., Quarteroni, A., & Zang, T. A. (2007). *Spectral methods: evolution to complex geometries and applications to fluid dynamics*. Springer Science & Business Media.

Cattell, C., Wygant, J., Goetz, K., Kersten, K., Kellogg, P., Von Rosenvinge, T., ... others (2008). Discovery of very large amplitude whistler-mode waves in earth's radiation belts. *Geophysical Research Letters*, *35*(1).

Chae, J., Cho, K., Nakariakov, V. M., Cho, K.-S., & Kwon, R.-Y. (2021). Spectroscopic detection of alfvénic waves in the chromosphere of sunspot regions. *The Astrophysical Journal Letters*, *914*(1), L16.

Chandran, B. D., Li, B., Rogers, B. N., Quataert, E., & Germaschewski, K. (2010). Perpendicular ion heating by low-frequency alfvén-wave turbulence in the solar wind. *The Astrophysical Journal*, *720*(1), 503.

Chaston, C., Bonnell, J., Carlson, C., McFadden, J., Ergun, R., Strangeway, R., & Lund, E. (2004). Auroral ion acceleration in dispersive alfvén waves. *Journal of Geophysical Research: Space Physics*, *109*(A4).

Chaston, C., Bonnell, J., Clausen, L., & Angelopoulos, V. (2012). Energy transport by kinetic-scale electromagnetic waves in fast plasma sheet flows. *Journal of Geophysical Research: Space Physics*, *117*(A9).

Chaston, C., Bonnell, J., Halford, A., Reeves, G. D., Baker, D., Kletzing, C., & Wygant, J. (2018). Pitch angle scattering and loss of radiation belt electrons in broadband electromagnetic waves. *Geophysical Research Letters*, *45*(18), 9344–9352.

Chaston, C., Bonnell, J., Wygant, J., Kletzing, C., Reeves, G. D., Gerrard, A., ... Smith, C. (2015). Extreme ionospheric ion energization and electron heating in alfvén waves in the storm time inner magnetosphere. *Geophysical Research Letters*, *42*(24), 10–531.

Chaston, C., Peticolas, L., Carlson, C., McFadden, J., Mozer, F., Wilber, M., ... others (2005). Energy deposition by alfvén waves into the dayside auroral oval: Cluster and fast observations. *Journal of Geophysical Research: Space Physics*, *110*(A2).

Chaston, C. C., Carlson, C. W., Ergun, R. E., & McFadden, J. P. (2000). Alfvén waves, density cavities and electron acceleration observed from the fast spacecraft. *Physica Scripta*, *2000*(T84), 64.

Chaston, C. C., Johnson, J. R., Wilber, M., Acuna, M., Goldstein, M. L., & Reme, H. (2009). Kinetic alfvén wave turbulence and transport through a reconnection diffusion region. *Physical Review Letters*, *102*(1), 015001.

Chaston, C. C., Phan, T. D., Bonnell, J. W., Mozer, F. S., Acuńa, M., Goldstein, M. L., et al. (2005). Drift-kinetic alfvén waves observed near a reconnection x line in the earth's magnetopause. *Physical Review Letters*, *95*(6), 065002.

Chen, C., Chandran, B., Woodham, L., Jones, S., Perez, J., Bourouaine, S., ... others (2021). The near-sun streamer belt solar wind: turbulence and solar wind acceleration. *Astronomy & Astrophysics*, *650*, L3.

Chen, C. H. K., Bale, S. D., Bonnell, J. W., Borovikov, D., Bowen, T. A., Burgess, D., & Whittlesey, P. (2020). The evolution and role of solar wind turbulence in the inner heliosphere. *The Astrophysical Journal Supplement Series*, *246*(2), 53.

Chen, L., Wu, D. J., & Hua, Y. P. (2011). Kinetic alfvén wave instability driven by a field-aligned current in high-β plasmas. *Physical Review E*, *84*(4), 046406.

Chen, L., Wu, D. J., & Huang, J. (2013). Kinetic alfvén wave instability driven by field-aligned currents in a low-β plasma. *Journal of Geophysical Research: Space Physics*, *118*(6), 2951-2957.

Chen, L., & Zonca, F. (2016). Physics of alfvén waves and energetic particles in burning plasmas. *Reviews of Modern Physics*, *88*(1), 015008.

Chen, L., Zonca, F., & Lin, Y. (2021). Physics of kinetic alfvén waves: a gyrokinetic theory approach. *Reviews of Modern Plasma Physics*, *5*, 1–37.

Cheng, Z. W., Zhang, J. C., Shi, J. K., Kistler, L. M., Dunlop, M., Dandouras, I., & Fazakerley, A. (2016). The particle carriers of field-aligned currents in the earth's magnetotail during a substorm. *Journal of Geophysical Research: Space Physics*, *121*(4), 3058–3068.

Cramer, N. F. (2011). *The physics of alfvén waves*. John Wiley & Sons.

Dai, L. (2009). Collisionless magnetic reconnection via alfvén eigenmodes. *Physical Review Letters*, *102*(24), 245003.

Dangelo, N., Joyce, G., & Pesses, M. E. (1979). Landau damping effects on solar wind fast streams. *Astrophysical Journal, Part 1, vol. 229, May 1, 1979, p. 1138-1142. NSF-supported research;*, *229*, 1138–1142.

Davidson, R. (2012). *Methods in nonlinear plasma theory*. Elsevier.

Del Zanna, L., & Velli, M. (2002). Coronal heating through alfvén waves. *Advances in Space Research*, *30*(3), 471–480.

Dewan, H., Singh, I., Uma, R., & Sharma, R. (2022). Numerical simulations to study nonlinear wave-based interaction and turbulent magnetic field ampli-

fication in the laboratory and astrophysical plasmas. *Plasma Physics and Controlled Fusion*, *64*(9), 095004.

Domingo, V. (2002). Soho, yohkoh, ulysses and trace: The four solar missions in perspective, and available resources. *Astrophysics and space science*, *282*, 171–188.

Doolen, G., DuBois, D., & Rose, H. A. (1985). Nucleation of cavitons in strong langmuir turbulence. *Physical review letters*, *54*(8), 804.

Duan, S., Dai, L., Wang, C., Liang, J., Lui, A., Chen, L., ... Angelopoulos, V. (2016). Evidence of kinetic alfvén eigenmode in the near-earth magnetotail during substorm expansion phase. *Journal of Geophysical Research: Space Physics*, *121*(5), 4316–4330.

Duan, S., Liu, Z., & Angelopoulos, V. (2012). Observations of kinetic alfvén waves by themis near a substorm onset. *Chinese science bulletin*, *57*, 1429–1435.

Dwivedi, N. K., Batra, K., & Sharma, R. (2012). Study of kinetic alfvén wave and whistler wave spectra and their implication in solar wind plasma. *Journal of Geophysical Research: Space Physics*, *117*(A7).

D'Amicis, R., Bruno, R., Panasenco, O., Telloni, D., Perrone, D., Marcucci, M. F., ... others (2021). First solar orbiter observation of the alfvénic slow wind and identification of its solar source. *Astronomy & Astrophysics*, *656*, A21.

D'Amicis, R., Perrone, D., Bruno, R., & Velli, M. (2021). *On alfvénic slow wind: A journey from the earth back to the sun.* Wiley Online Library.

Escande, D. F., Gondret, V., & Sattin, F. (2019). Relevant heating of the quiet solar corona by alfvén waves: a result of adiabaticity breakdown. *Scientific reports*, *9*(1), 14274.

Fiksel, G., Almagri, A., Chapman, B., Mirnov, V., Ren, Y., Sarff, J., & Terry, P. (2009). Mass-dependent ion heating during magnetic reconnection in a laboratory plasma. *Physical review letters*, *103*(14), 145002.

Fisk, L. A. (2003). Acceleration of the solar wind as a result of the reconnection of open magnetic flux with coronal loops. *Journal of Geophysical Research: Space Physics*, *108*(A4).

Fornberg, B., & Whitham, G. B. (1978). A numerical and theoretical study of certain nonlinear wave phenomena. *Philosophical Transactions of the Royal Society of London. Series A, Mathematical and Physical Sciences*, *289*(1361), 373–404.

Fuchs, V., Cairns, R., Shoucri, M., Hizanidis, K., & Bers, A. (1985). A one-dimensional model for lower-hybrid current drive including perpendicular dynamics. *The Physics of fluids*, *28*(12), 3619–3628.

Gary, S. P., & Nishimura, K. (2004). Kinetic alfvén waves: Linear theory and a particle-in-cell simulation. *Journal of Geophysical Research: Space Physics*, *109*(A2).

Gekelman, W. (1999). Review of laboratory experiments on alfvén waves and their relationship to space observations. *Journal of Geophysical Research: Space Physics*, *104*(A7), 14417–14435.

Génot, V., Louarn, P., & Mottez, F. (2000). Electron acceleration by alfvén waves in density cavities. *Journal of Geophysical Research: Space Physics*, *105*(A12), 27611–27620.

Gershman, D. J., F-Viñas, A., Dorelli, J. C., Boardsen, S. A., Avanov, L. A., Bellan, P. M., ... others (2017). Wave-particle energy exchange directly observed in a kinetic alfvén-branch wave. *Nature communications*, *8*(1), 14719.

Goertz, C. K., & Boswell, R. W. (1979). Magnetosphere-ionosphere coupling. *Journal of Geophysical Research: Space Physics*, *84*(A12), 7239–7246.

Goossens, M., Erdélyi, R., & Ruderman, M. S. (2011). Resonant mhd waves in the solar atmosphere. *Space Science Reviews*, *158*, 289–338.

Goyal, R., Sharma, R., & Gupta, D. (2018). Whistler mode localization and turbulence implicating particle acceleration in radiation belts. *Physics of Plasmas*,

25(12).

Grant, S. D., Jess, D. B., Zaqarashvili, T. V., Beck, C., Socas-Navarro, H., Aschwanden, M. J., ... Hewitt, R. L. (2018). Alfvén wave dissipation in the solar chromosphere. *Nature Physics*, *14*(5), 480–483.

Hasegawa, A. (1976). Particle acceleration by mhd surface wave and formation of aurora. *Journal of Geophysical Research*, *81*(28), 5083–5090.

Hasegawa, A., & Mima, K. (1976). Exact solitary alfvén wave. *Physical Review Letters*, *37*(11), 690.

Heyvaerts, J., & Priest, E. R. (1983). Coronal heating by phase-mixed shear alfvén waves. *Astronomy and Astrophysics*, *117*(2), 220–234.

Hollweg, J. V. (1999). Kinetic alfvén wave revisited. *Journal of Geophysical Research: Space Physics*, *104*(A7), 14811–14819.

Hoppock, I. W., Chandran, B. D., Klein, K. G., Mallet, A., & Verscharen, D. (2018). Stochastic proton heating by kinetic-alfvén-wave turbulence in moderately high-plasmas. *Journal of plasma physics*, *84*(6), 905840615.

Howes, G. G., Cowley, S. C., Dorland, W., Hammett, G. W., Quataert, E., & Schekochihin, A. A. (2006). Astrophysical gyrokinetics: basic equations and linear theory. *The Astrophysical Journal*, *651*(1), 590.

Huang, S., Sahraoui, F., Andrés, N., Hadid, L., Yuan, Z., He, J., ... others (2021). The ion transition range of solar wind turbulence in the inner heliosphere: Parker solar probe observations. *The Astrophysical journal letters*, *909*(1), L7.

Hudson, H. (1991). Solar flares, microflares, nanoflares, and coronal heating. *Solar Physics*, *133*, 357–369.

Ichimaru, S., & Yakimenko, I. (1973). Transition probability approach to the theory of plasmas. *Physica Scripta*, *7*(5), 198.

Johns Hopkins University Applied Physics Laboratory. (2023). *Parker solar probe - the mission.* Retrieved from `https://parkersolarprobe.jhuapl.edu/`

Johnson, J. R., & Cheng, C. (2001). Stochastic ion heating at the magnetopause due to kinetic alfvén waves. *Geophysical research letters*, *28*(23), 4421–4424.

Johnson, J. R., Cheng, C., & Song, P. (2001). Signatures of mode conversion and kinetic alfvén waves at the magnetopause. *Geophysical Research Letters*, *28*(2), 227–230.

Johnson, J. R., & Cheng, C. Z. (1997). Kinetic alfvén waves and plasma transport at the magnetopause. *Geophysical Research Letters*, *24*(11), 1423–1426.

Kasper, J., Klein, K., Lichko, E., Huang, J., Chen, C., Badman, S., ... others (2021). Parker solar probe enters the magnetically dominated solar corona. *Physical review letters*, *127*(25), 255101.

Kaur, N., & Saini, N. S. (2016). Ion acoustic kinetic alfvén rogue waves in two temperature electrons superthermal plasmas. *Astrophysics and Space Science*, *361*(10), 331.

Keiling, A., Parks, G., Wygant, J., Dombeck, J., Mozer, F., Russell, C., ... Lotko, W. (2005). Some properties of alfvén waves: Observations in the tail lobes and the plasma sheet boundary layer. *Journal of Geophysical Research: Space Physics*, *110*(A10).

Kopriva, D. A. (2009). *Implementing spectral methods for partial differential equations: Algorithms for scientists and engineers.* Springer Science & Business Media.

Kumar, S., Sharma, R., & Singh, H. (2009). Nonlinear excitation of short scale turbulence in solar corona by kinetic alfvén waves. *Physics of Plasmas*, *16*(7).

Larosa, A. (2021). *Constraints on the switchbacks generation mechanisms and modeling of the slow extraordinary modes magnetic signatures: Parker solar probe observations* (Unpublished doctoral dissertation). Université d'Orléans.

Leamon, R. J., Smith, C. W., Ness, N. F., Matthaeus, W. H., & Wong, H. K. (1998). Observational constraints on the dynamics of the interplanetary magnetic field dissipation range. *Journal of Geophysical Research: Space Physics*,

103(A3), 4775–4787.

Liewer, P. C., Vourlidas, A., Stenborg, G., Howard, R. A., Qiu, J., Penteado, P., ... Braga, C. R. (2023). Structure of the plasma near the heliospheric current sheet as seen by wispr/parker solar probe from inside the streamer belt. *The Astrophysical Journal*, *948*(1), 24.

Lion, S., Alexandrova, O., & Zaslavsky, A. (2016). Coherent events and spectral shape at ion kinetic scales in the fast solar wind turbulence. *The Astrophysical Journal*, *824*(1), 47.

Liu, Z.-Y., Zong, Q.-G., Rankin, R., Zhang, H., Hao, Y.-X., He, J.-S., ... others (2023). Particle-sounding of the spatial structure of kinetic alfvén waves. *Nature Communications*, *14*(1), 2088.

López, R. A., Viñas, A. F., Araneda, J. A., & Yoon, P. H. (2017). Kinetic scale structure of low-frequency waves and fluctuations. *The Astrophysical Journal*, *845*(1), 60.

Lotz, S., Nel, A., Wicks, R., Roberts, O., Engelbrecht, N., Strauss, R., ... Bale, S. (2023). The radial variation of the solar wind turbulence spectra near the kinetic break scale from parker solar probe measurements. *The Astrophysical Journal*, *942*(2), 93.

Lysak, R., Hudson, M., & Temerin, M. (1980). Ion heating by strong electrostatic ion cyclotron turbulence. *Journal of Geophysical Research: Space Physics*, *85*(A2), 678–686.

Malara, F., Nigro, G., Valentini, F., & Sorriso-Valvo, L. (2019). Electron heating by kinetic alfvén waves in coronal loop turbulence. *The Astrophysical Journal*, *871*(1), 66.

Malaspina, D. M., Stenborg, G., Mehoke, D., Al-Ghazwi, A., Shen, M. M., Hsu, H.-W., ... de Wit, T. D. (2022). Clouds of spacecraft debris liberated by hypervelocity dust impacts on parker solar probe. *The Astrophysical Journal*, *925*(1), 27.

Markovskii, S., Vasquez, B. J., Smith, C. W., & Hollweg, J. V. (2006). Dissipation of the perpendicular turbulent cascade in the solar wind. *The Astrophysical Journal*, *639*(2), 1177.

Matteini, L., Franci, L., Alexandrova, O., Lacombe, C., Landi, S., Hellinger, P., ... Verdini, A. (2020). Magnetic field turbulence in the solar wind at sub-ion scales: In situ observations and numerical simulations. *Frontiers in Astronomy and Space Sciences*, *7*, 563075.

Matthaeus, W. H., Zank, G. P., Oughton, S., Mullan, D. J., & Dmitruk, P. (1999). Coronal heating by magnetohydrodynamic turbulence driven by reflected low-frequency waves. *The Astrophysical Journal*, *523*(1), L93.

McComas, D. J., Velli, M., Lewis, W. S., Acton, L. W., Balat-Pichelin, M., Bothmer, V., et al. (2007). Understanding coronal heating and solar wind acceleration: Case for in situ near-sun measurements. *Reviews of Geophysics*, *45*(1).

Moya, P. S., Pinto, V. A., Viñas, A. F., Sibeck, D. G., Kurth, W. S., Hospodarsky, G. B., & Wygant, J. R. (2015). Weak kinetic alfvén waves turbulence during the 14 november 2012 geomagnetic storm: Van allen probes observations. *Journal of Geophysical Research: Space Physics*, *120*(7), 5504–5523.

Nättilä, J., & Beloborodov, A. M. (2022). Heating of magnetically dominated plasma by alfvén-wave turbulence. *Physical Review Letters*, *128*(7), 075101.

Passot, T., Henri, P., Laveder, D., & Sulem, P.-L. (2014). Fluid simulations of ion scale plasmas with weakly distorted magnetic fields: Flr-landau fluid simulations. *The European Physical Journal D*, *68*, 1–9.

Patterson Jr, G., & Orszag, S. A. (1971). Spectral calculations of isotropic turbulence: Efficient removal of aliasing interactions. *The Physics of Fluids*, *14*(11), 2538–2541.

Phillips, K. J. (2000). Why is the sun's corona so hot? views from soho, yohkoh and solar eclipses. *Plasma physics and controlled fusion*, *42*(2), 113.

Podesta, J. (2011). On the energy cascade rate of solar wind turbulence in high cross helicity flows. *Journal of Geophysical Research: Space Physics*, *116*(A5).

Popel, S., Vladimirov, S., & Shukla, P. (1995). Ion-acoustic solitons in electron–positron–ion plasmas. *Physics of Plasmas*, *2*(3), 716–719.

Raghav, A. N., & Kule, A. (2018). Does the alfvén wave disrupt the large-scale magnetic cloud structure? *Monthly Notices of the Royal Astronomical Society: Letters*, *480*(1), L6–L11.

Rai, R. K., Sharma, S., Yadav, N., & Sharma, R. P. (2017). Nonlinear effects associated with kinetic alfvén wave in magnetic islands. *Physics of Plasmas*, *24*(1).

Ripoll, J.-F., Claudepierre, S., Ukhorskiy, A., Colpitts, C., Li, X., Fennell, J., & Crabtree, C. (2020). Particle dynamics in the earth's radiation belts: Review of current research and open questions. *Journal of Geophysical Research: Space Physics*, *125*(5), e2019JA026735.

Roberts, D. A. (1990). Heliocentric distance and temporal dependence of the interplanetary density-magnetic field magnitude correlation. *Journal of Geophysical Research: Space Physics*, *95*(A2), 1087-1090.

Rozmus, W., Sharma, R., Samson, J., & Tighe, W. (1987). Nonlinear evolution of stimulated raman scattering in homogeneous plasmas. *The Physics of fluids*, *30*(7), 2181–2193.

Sadiq, N., Ahmad, M., Farooq, M., & Jan, Q. (2018a). Linear and nonlinear analysis of kinetic alfven waves in quantum magneto-plasmas with arbitrary temperature degeneracy. *Physics of Plasmas*, *25*(6).

Sadiq, N., Ahmad, M., Farooq, M., & Jan, Q. (2018b). Linear and nonlinear analysis of kinetic alfven waves in quantum magneto-plasmas with arbitrary temperature degeneracy. *Physics of Plasmas*, *25*(6).

Sahraoui, F., Belmont, G., Goldstein, M. L., & Rezeau, L. (2010). Limitations of multispacecraft data techniques in measuring wave number spectra of space plasma turbulence. *Journal of Geophysical Research: Space Physics*, *115*(A4).

Sahraoui, F., Goldstein, M., Robert, P., & Khotyaintsev, Y. V. (2009). Evidence of a cascade and dissipation of solar-wind turbulence at the electron gyroscale. *Physical review letters*, *102*(23), 231102.

Saleem, H., & Mahmood, S. (2003). Shear alfven wave density dips in electron-positron-ion plasmas. *Physics of Plasmas*, *10*(6), 2612–2615.

Salem, C. S., Howes, G. G., Sundkvist, D., Bale, S. D., Chaston, C. C., Chen, C. H. K., & Mozer, F. S. (2012). Identification of kinetic alfvén wave turbulence in the solar wind. *The Astrophysical Journal Letters*, *745*(1), L9.

Schekochihin, A. A., Cowley, S. C., Dorland, W., Hammett, G. W., Howes, G. G., Quataert, E., & Tatsuno, T. (2009). Astrophysical gyrokinetics: kinetic and fluid turbulent cascades in magnetized weakly collisional plasmas. *The Astrophysical Journal Supplement Series*, *182*(1), 310.

Shaikh, D., & Zank, G. (2009). Spectral features of solar wind turbulent plasma. *Monthly notices of the royal astronomical society*, *400*(4), 1881–1891.

Sharma, R., & Kumar, S. (2010). Kinetic alfvén wave turbulence in space plasmas. *Physics Letters A*, *374*(34), 3491–3498.

Sharma, R., Stubbe, P., & Verga, A. (1996). Numerical simulation of a zakharov-boussinesq system of equations to study langmuir turbulence in the ionosphere. *Journal of Geophysical Research: Space Physics*, *101*(A5), 10995–11003.

Sharma Pyakurel, P., Shay, M. A., Haggerty, C. C., Parashar, T., Drake, J. F., Cassak, P., & Gary, S. P. (2018). Super-alfvénic propagation and damping of reconnection onset signatures. *Journal of Geophysical Research: Space Physics*, *123*(1), 341–349.

Shen, Y., & Knudsen, D. J. (2020). On o+ ion heating by bbelf waves at low altitude: Test particle simulations. *Journal of Geophysical Research: Space Physics*, *125*(8), e2019JA027291.

Shi, C., Zhao, J., Huang, J., Wang, T., Wu, D., Chen, Y., & Bale, S. D. (2021).

Parker solar probe observations of alfvénic waves and ion-cyclotron waves in a small-scale flux rope. *The Astrophysical Journal Letters*, *908*(1), L19.

Shukla, N., Varma, P., & Tiwari, M. S. (2009). Study on kinetic alfven wave in inertial regime. *No Journal Provided*. (Citation without a journal reference)

Shukla, P., & Stenflo, L. (2000a). Generation of localized density perturbations by shear alfvén waves. *Physics of Plasmas*, *7*(6), 2738–2739.

Shukla, P., & Stenflo, L. (2000b). Nonlinear phenomena involving dispersive alfvén waves. In *Nonlinear mhd waves and turbulence: Proceeding of the workshop held in nice, france, 1–4 december 1998* (pp. 1–30).

Shukla, P., Stenflo, L., & Bingham, R. (1999). Nonlinear propagation of inertial alfvén waves in auroral plasmas. *Physics of Plasmas*, *6*(5), 1677–1680.

Shukla, P. K., & Stenflo, L. (2005). Decay of a magnetic-field-aligned alfvén wave into inertial and kinetic alfvén waves in plasmas. *Physics of Plasmas*, *12*(8).

Shukla, P. K., Stenflo, L., Bingham, R., & Eliasson, B. (2004). Nonlinear effects associated with dispersive alfvén waves in plasmas. *Plasma physics and controlled fusion*, *46*(12B), B349.

Simnett, G. (2005). Near-relativistic electron emission following the 28 october 2003 x17 flare. *Journal of Geophysical Research: Space Physics*, *110*(A9).

Singh, H., & Sharma, R. (2006). Numerical simulation of kinetic alfvén waves to study filament formation and their nonlinear dynamics in solar wind and corona. *Physics of plasmas*, *13*(1).

Singh, H. D., & Jatav, B. S. (2019). Anisotropic turbulence of kinetic alfvén waves and heating in solar corona. *Research in Astronomy and Astrophysics*, *19*(12), 185.

Singh, I., Uma, R., & Sharma, R. (2022). A nonlinear wave-based model to study the magnetic turbulence generation associated with the nonlinear evolution of kinetic alfven wave in laser-produced plasma relevant to laboratory and astrophysical plasmas. *Optik*, *267*, 169698.

Singh, M., Singh, K., & Saini, N. S. (2021). Large-amplitude dust inertial alfvén waves in an electron-depleted dusty plasma. *Pramana*, *95*, 1-9.

Sinhababu, A., & Ayyalasomayajula, S. (2021). Accuracy and computational efficiency of dealiasing schemes for the dns of under resolved flows with strong gradients. *Mathematics and Computers in Simulation*, *182*, 116–142.

Smith, C. W., Hamilton, K., Vasquez, B. J., & Leamon, R. J. (2006). Dependence of the dissipation range spectrum of interplanetary magnetic fluctuationson the rate of energy cascade. *The Astrophysical Journal*, *645*(1), L85.

Song, P., & Vasyliūnas, V. M. (2011). Heating of the solar atmosphere by strong damping of alfvén waves. *Journal of Geophysical Research: Space Physics*, *116*(A9).

Stasiewicz, K., Bellan, P., Chaston, C., Kletzing, C., Lysak, R., Maggs, J., ... others (2000). Small scale alfvénic structure in the aurora. *Space Science Reviews*, *92*, 423–533.

Stéfant, R. J. (1970). Alfvén wave damping from finite gyroradius coupling to the ion acoustic mode. *The Physics of Fluids*, *13*(2), 440–450.

Suzuki, T. K., & Inutsuka, S.-i. (2006). Solar winds driven by nonlinear low-frequency alfvén waves from the photosphere: Parametric study for fast/slow winds and disappearance of solar winds. *Journal of Geophysical Research: Space Physics*, *111*(A6).

Telloni, D., Sorriso-Valvo, L., Woodham, L. D., Panasenco, O., Velli, M., Carbone, F., & Angelini, V. (2021). Evolution of solar wind turbulence from 0.1 to 1 au during the first parker solar probe–solar orbiter radial alignment. *The Astrophysical Journal Letters*, *912*(2), L21.

Terres, M., & Li, G. (2022). Relating the solar wind turbulence spectral break at the dissipation range with an upstream spectral bump at planetary bow shocks. *The Astrophysical Journal*, *924*(2), 53.

Tsiklauri, D. (2006). A fresh look at the heating mechanisms of the solar corona. *New Journal of Physics*, *8*(5), 79.

Tsiklauri, D. (2012). Three dimensional particle-in-cell simulation of particle acceleration by circularly polarised inertial alfven waves in a transversely inhomogeneous plasma. *Physics of Plasmas*, *19*(8).

Tu, C.-Y., & Marsch, E. (2001). On cyclotron wave heating and acceleration of solar wind ions in the outer corona. *Journal of Geophysical Research: Space Physics*, *106*(A5), 8233–8252.

Velli, M. (2003). Mhd turbulence and the heating of astrophysical plasmas. *Plasma physics and controlled fusion*, *45*(12A), A205.

Velli, M., Pucci, F., Rappazzo, F., & Tenerani, A. (2015). Models of coronal heating, turbulence and fast reconnection. *Philosophical Transactions of the Royal Society A: Mathematical, Physical and Engineering Sciences*, *373*(2042), 20140262.

Wu, D., Feng, H., Li, B., & He, J. (2016). Nature of turbulence, dissipation, and heating in space plasmas: From alfvén waves to kinetic alfvén waves. *Journal of Geophysical Research: Space Physics*, *121*(8), 7349–7352.

Xu, S., Huang, S., Sahraoui, F., Yuan, Z., Wu, H., Jiang, K., ... Lin, R. (2023). Observations of kolmogorov turbulence in saturn's magnetosphere. *Geophysical Research Letters*, *50*(16), e2023GL105463.

Yadav, N., & Sharma, R. (2014). Nonlinear interaction of 3d kinetic alfvén waves and ion acoustic waves in solar wind plasmas. *Solar Physics*, *289*, 1803–1814.

Yin, Z., Yuan, L., & Tang, T. (2005). A new parallel strategy for two-dimensional incompressible flow simulations using pseudo-spectral methods. *Journal of Computational Physics*, *210*(1), 325–341.

Yinhua, C., Wei, L., & Yu, M. (2000). Nonlinear dust kinetic alfvén waves. *Physical Review E*, *61*(1), 809.

Zhang, L., Wang, C., Dai, L., Ren, Y., & Lui, A. (2022). A statistical study on wide-amplitude kinetic alfvénic pulse at 8–12re in the magnetotail by themis spacecraft from 2008 to 2010. *Journal of Geophysical Research: Space Physics*, *127*(2), e2021JA029593.

Zhao, L.-L., Zank, G., Adhikari, L., Telloni, D., Stevens, M., Kasper, J., ... Raouafi, N. (2022). Turbulence and waves in the sub-alfvénic solar wind observed by the parker solar probe during encounter 10. *The Astrophysical Journal Letters*, *934*(2), L36.

Zhao, L.-L., Zank, G., Telloni, D., Stevens, M., Kasper, J., & Bale, S. (2022). The turbulent properties of the sub-alfvénic solar wind measured by the parker solar probe. *The Astrophysical Journal Letters*, *928*(2), L15.

Šafránková, J., Němeček, Z., Němec, F., Verscharen, D., Horbury, T. S., Bale, S. D., & Přech, L. (2023). Evolution of magnetic field fluctuations and their spectral properties within the heliosphere: Statistical approach. *The Astrophysical Journal Letters*, *946*(2), L44.

Table 1. Simulation Parameters for Radiation Belt and near-Sun Streamer Belt Solar wind

	Radiation Belt	Streamer Belt		Radiation Belt	Streamer Belt
ρ_i	2.04×10^6 cm	1.34×10^6 cm	c_1	0.93436342	0.00049027
ρ_s	6.5×10^5 cm	1.90×10^6 cm	c_2	0.19143023	0.00048930
v_A	4.877×10^8 cm/s	3.45×10^6 cm/s	c_3	0.14374822	0.00007543
c_s	9.785×10^7 cm/s	6.42×10^6 cm/s	c_4	0.13431308	0.00000004
v_{te}	1.349×10^9 cm/s	3.89×10^8 cm/s	c_5	0.81813534	0.00000096
k_{0z}	2.005×10^{-9} cm^{-1}	5.99×10^{-8} cm^{-1}	c_6	0.15661584	0.00000000
k_{0x}	8.416×10^{-7} cm^{-1}	1.19×10^{-5} cm^{-1}	c_7	0.16761769	0.00000096
x_n	6.359×10^5 cm	8.57×10^7 cm	c_8	0.87560720	0.00195724
z_n	1.302×10^9 cm	1.71×10^{10} cm	c_9	0.02451409	0.00000310
t_n	2.084 s	4.67 s			
B_n	4.013×10^{-2} G	1.286×10^{-2} G			

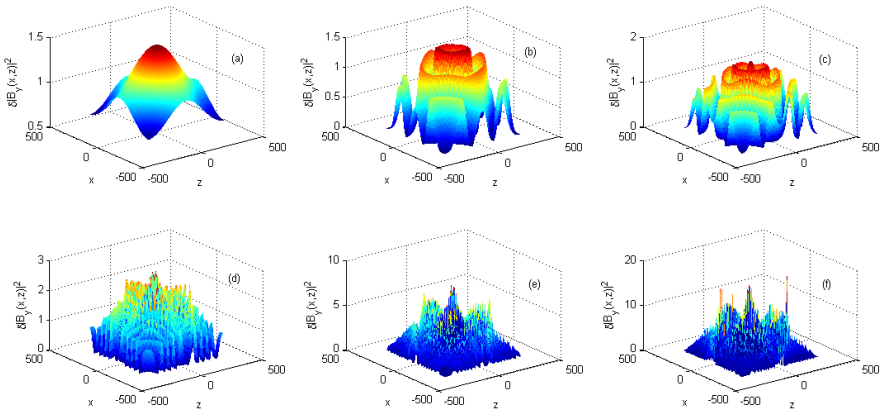

Figure 1. Snapshots of fluctuating magnetic field intensity profiles of KAWs at (a) $t = 0.5$, (b) $t = 13$, (c) $t = 18$, (d) $t = 44$, (e) $t = 75$ and (f) $t = 95$.

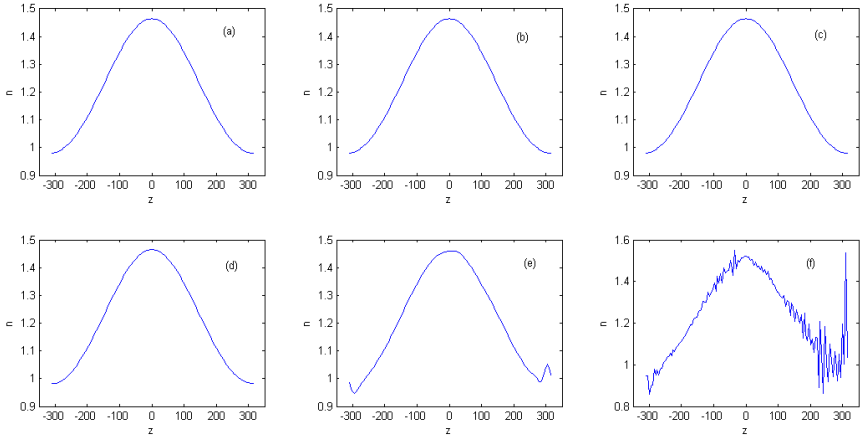

Figure 2. Density fluctuations along $z-$ direction at different times applicable for the Earth's radiation belt: (a), (b), (c), (d), (e) and (f) corresponds to the density fluctuations at time $t = 0.5, 13, 18, 44, 75,$ and 95 respectively.

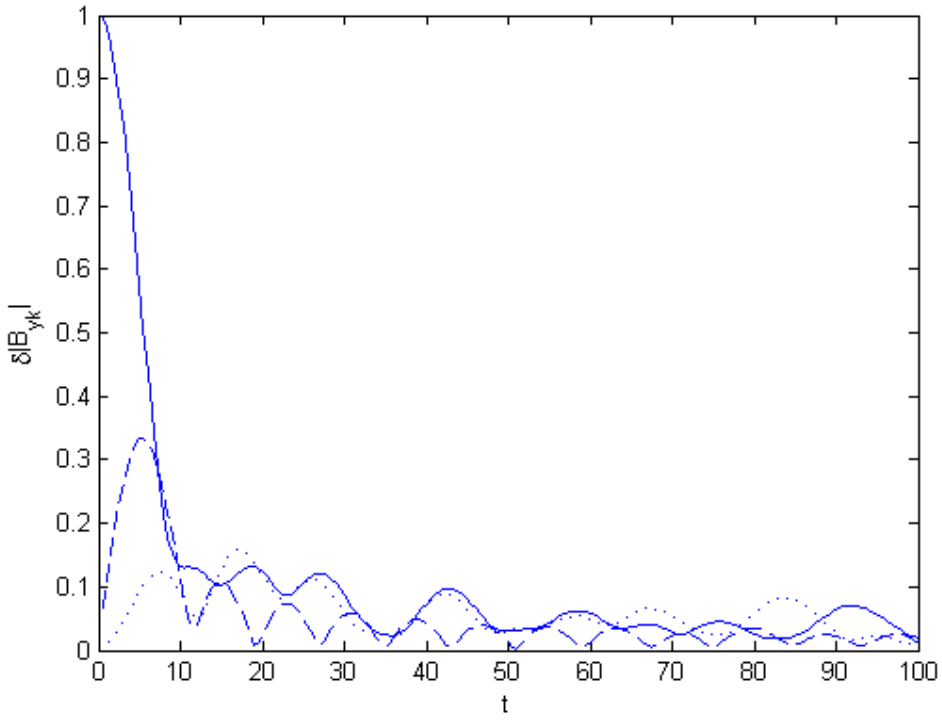

Figure 3. Evolution of the magnetic field in Fourier mode across three distinct modes: Mode A (solid line with $k_x = 1$, $k_z = 0$), Mode B (dashed line with $k_x = 2$, $k_z = 0$) and Mode C (dotted line with $k_x = 3$, $k_z = 0$).

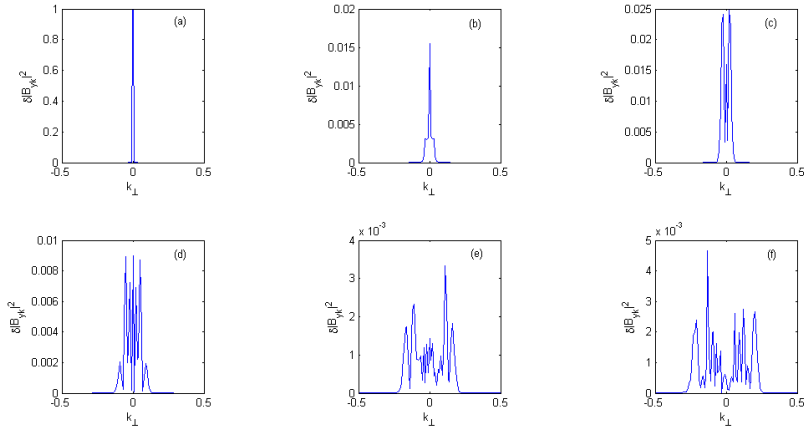

Figure 4. Distribution of magnetic energy across various wavenumbers at six different times: (a), (b), (c), (d), (e) and (f) with $t = 0.5, 13, 18, 44, 75$ and 95 respectively. Initially, at $t = 0.5$ only a single wave mode exists, but higher harmonics are generated at later times.

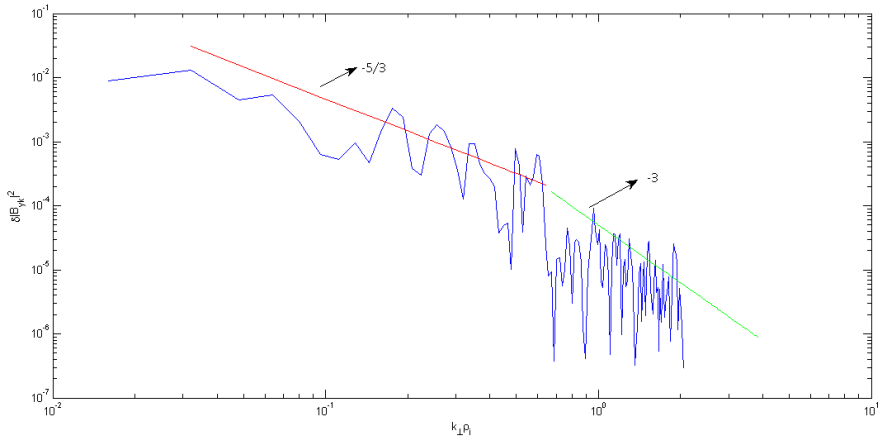

Figure 5. The fluctuating magnetic power spectrum $|\delta B_{yk}|^2$ versus $k_\perp \rho_i$ plotted at $t = 95$ for the Earth's radiation belt plasma, $\beta < 1$.

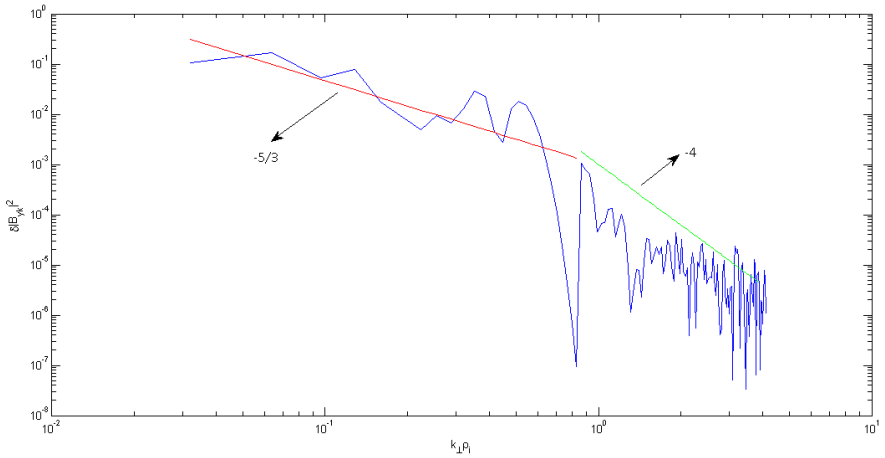

Figure 6. The fluctuating magnetic power spectrum $|\delta B_{yk}|^2$ versus $k_\perp \rho_i$ plotted at $t = 76$ for near-Sun streamer belt solar wind plasma, $\beta > 1$.

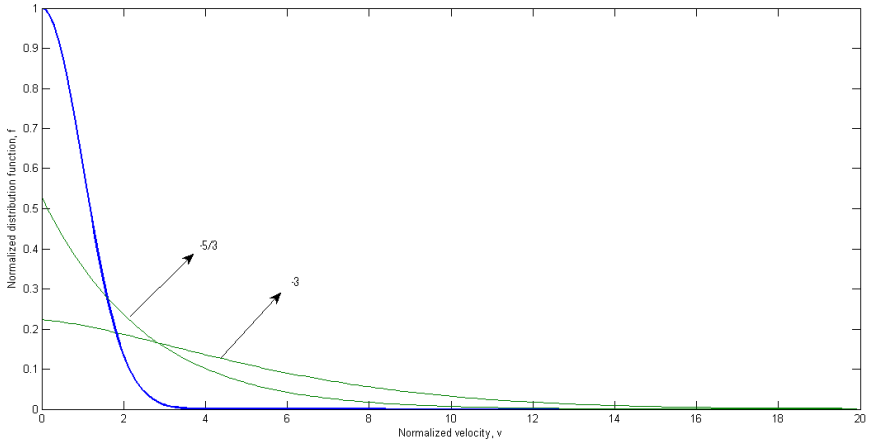

Figure 7. Normalized particle distribution function at scaled times $\tau = 0$ (blue) and $\tau = 30$ for spectral indices $-5/3$ and -3 showing the development of a superthermal tail due to stochastic heating by fluctuating fields.

Fig1.

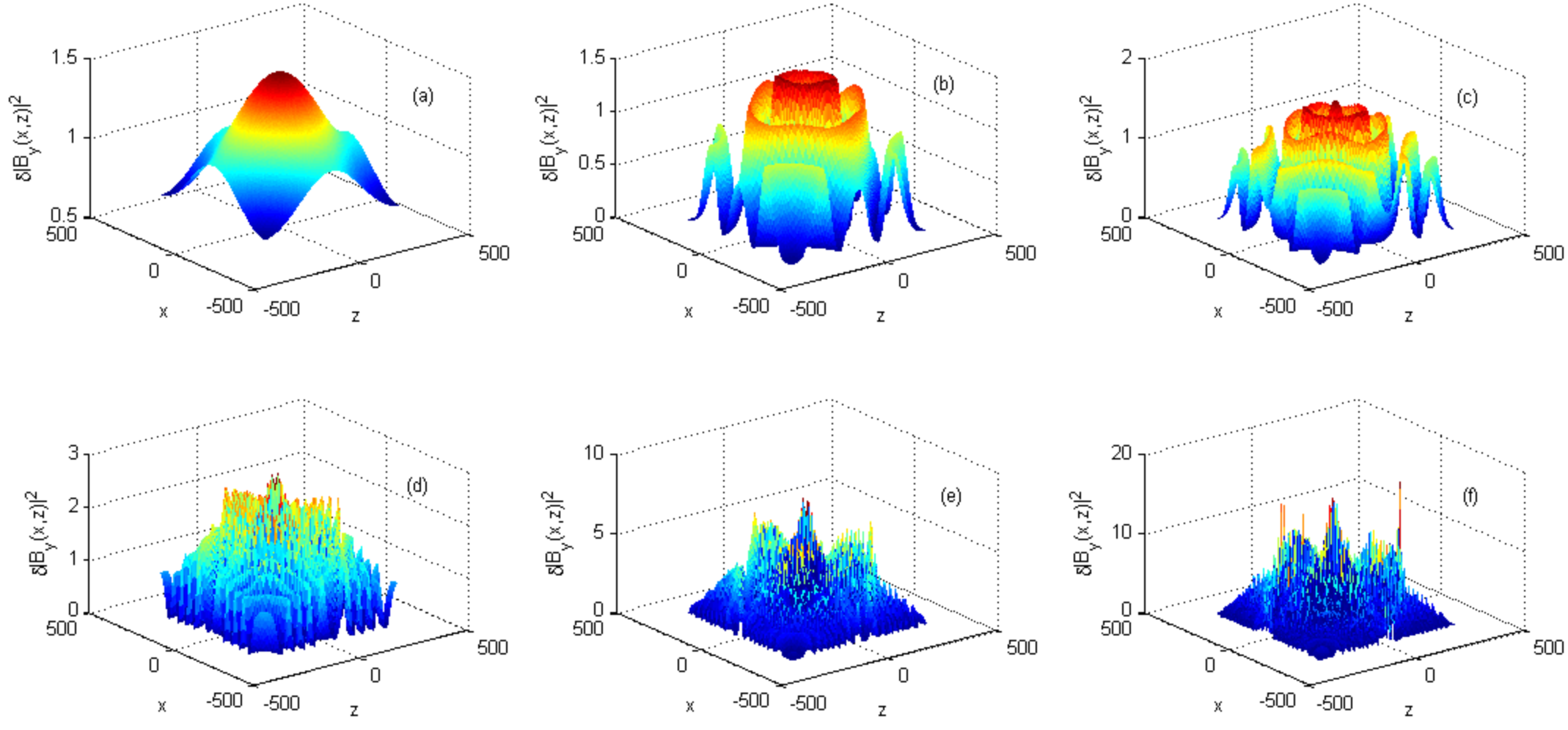
(a)
(b)
(c)
(d)
(e)
(f)
δ|B_y(x,z)|^2
x
z
500
0
-500

Fig2.

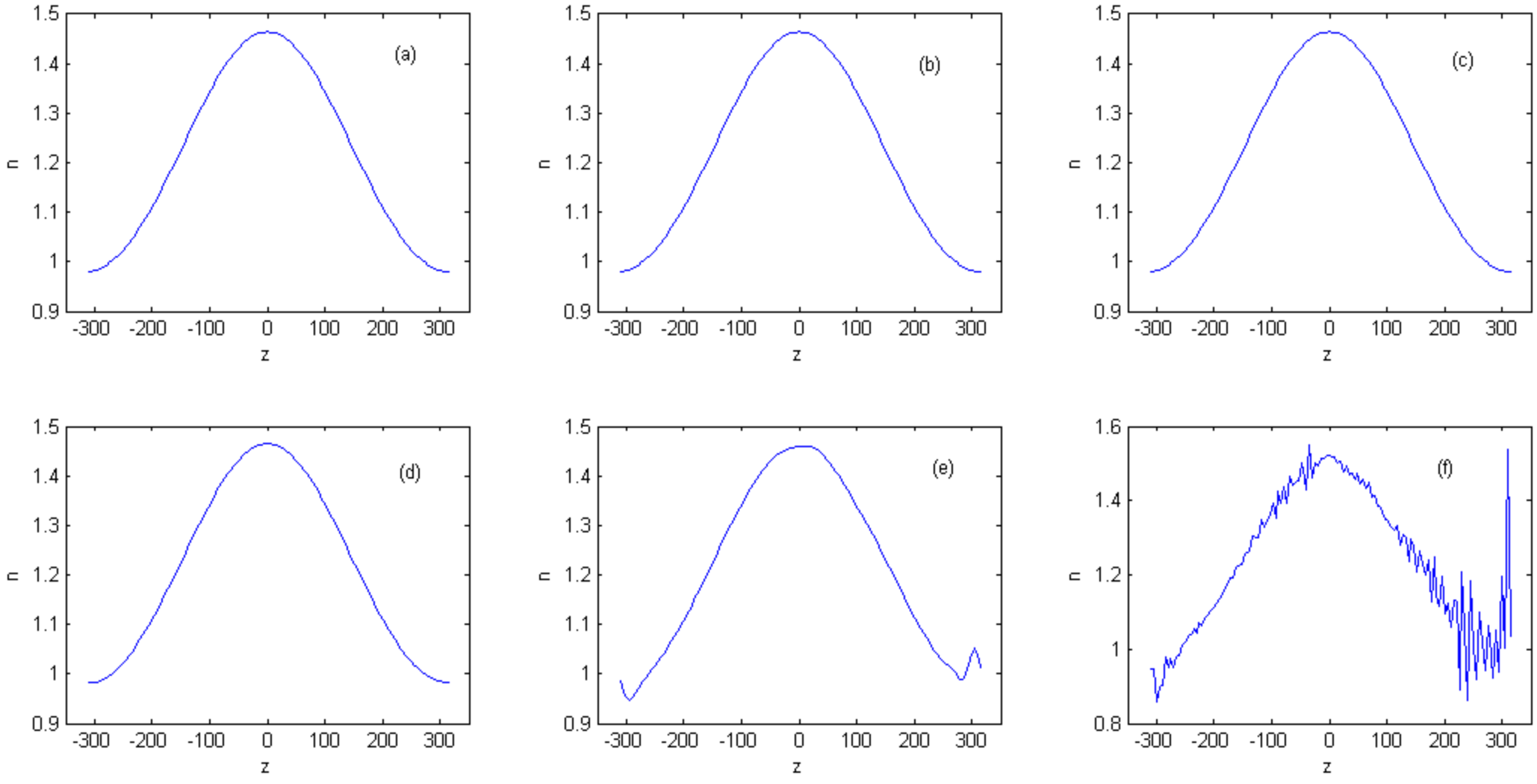
(a)
(b)
(c)
(d)
(e)
(f)
n
z
1.5
1.4
1.3
1.2
1.1
1
0.9
1.6
0.8
-300
-200
-100
0
100
200
300

Fig3.

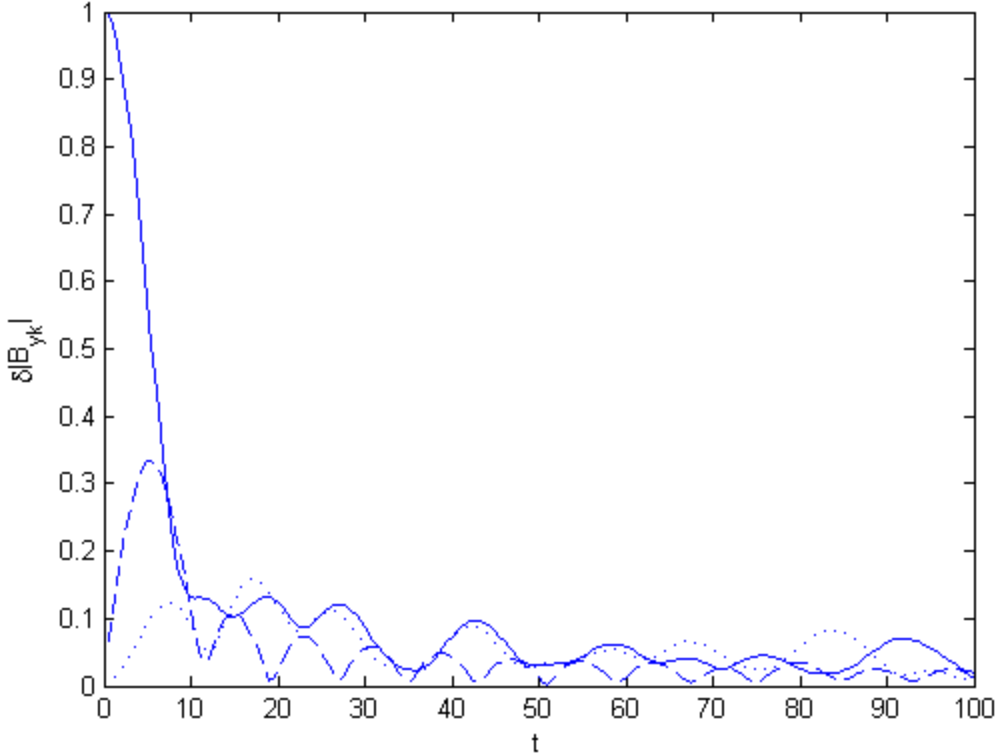
1
0.9
0.8
0.7
0.6
0.5
0.4
0.3
0.2
0.1
0
δ|B_yk|
0
10
20
30
40
50
60
70
80
90
100
t

Fig4.

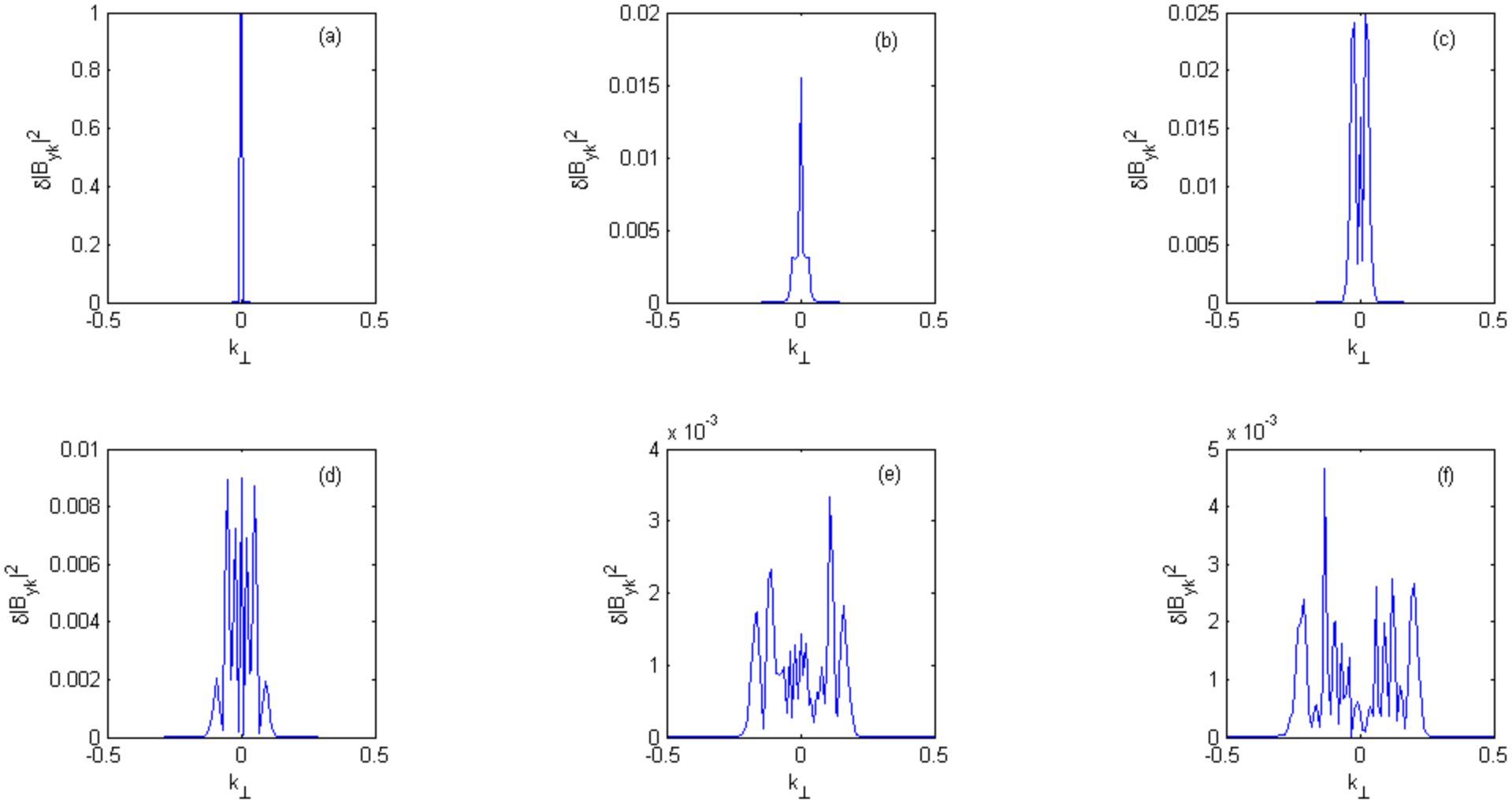
(a)
(b)
(c)
(d)
(e)
(f)
$\delta|B_{yk}|^2$
$k_\perp$
x 10^{-3}

Fig5.

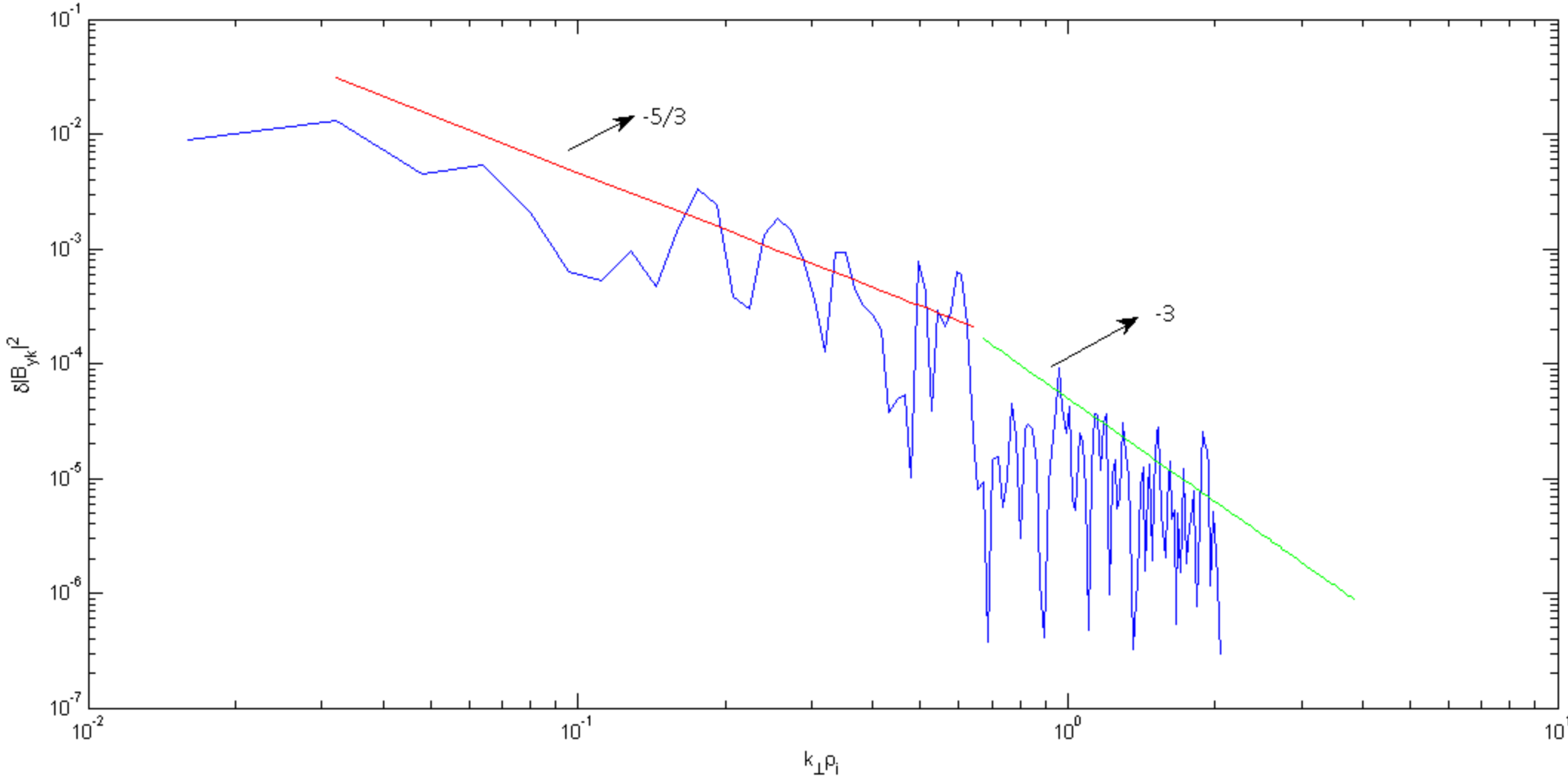
-5/3
-3
$\delta|B_{yk}|^2$
$k_\perp\rho_i$
10^{-1}
10^{-2}
10^{-3}
10^{-4}
10^{-5}
10^{-6}
10^{-7}
10^{-2}
10^{-1}
10^{0}
10^{1}

Fig6.

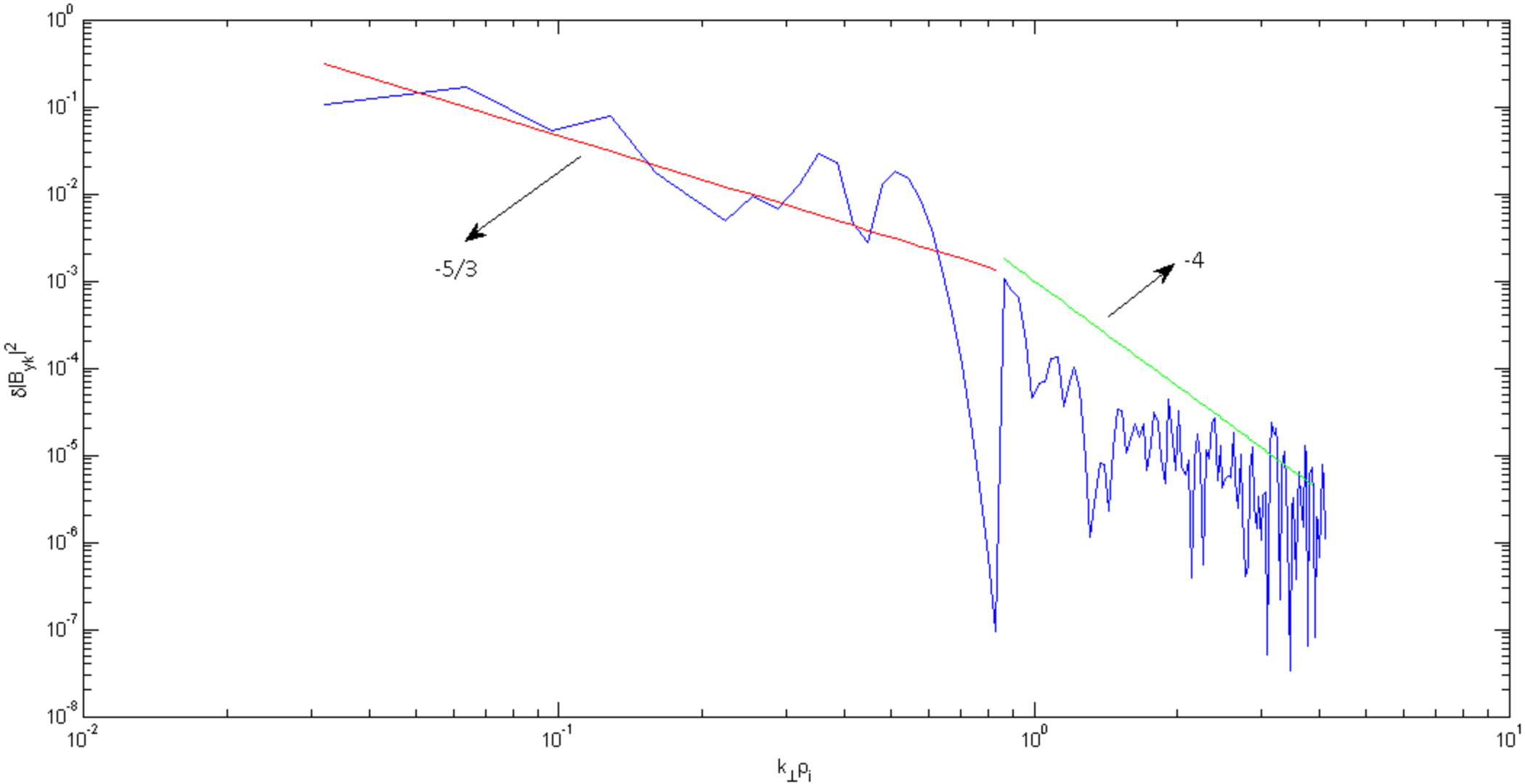
10^{0}
10^{-1}
10^{-2}
10^{-3}
10^{-4}
10^{-5}
10^{-6}
10^{-7}
10^{-8}
$\delta|B_{yk}|^2$
10^{-2}
10^{-1}
10^{0}
10^{1}
$k_\perp \rho_i$
-5/3
-4

Fig7.

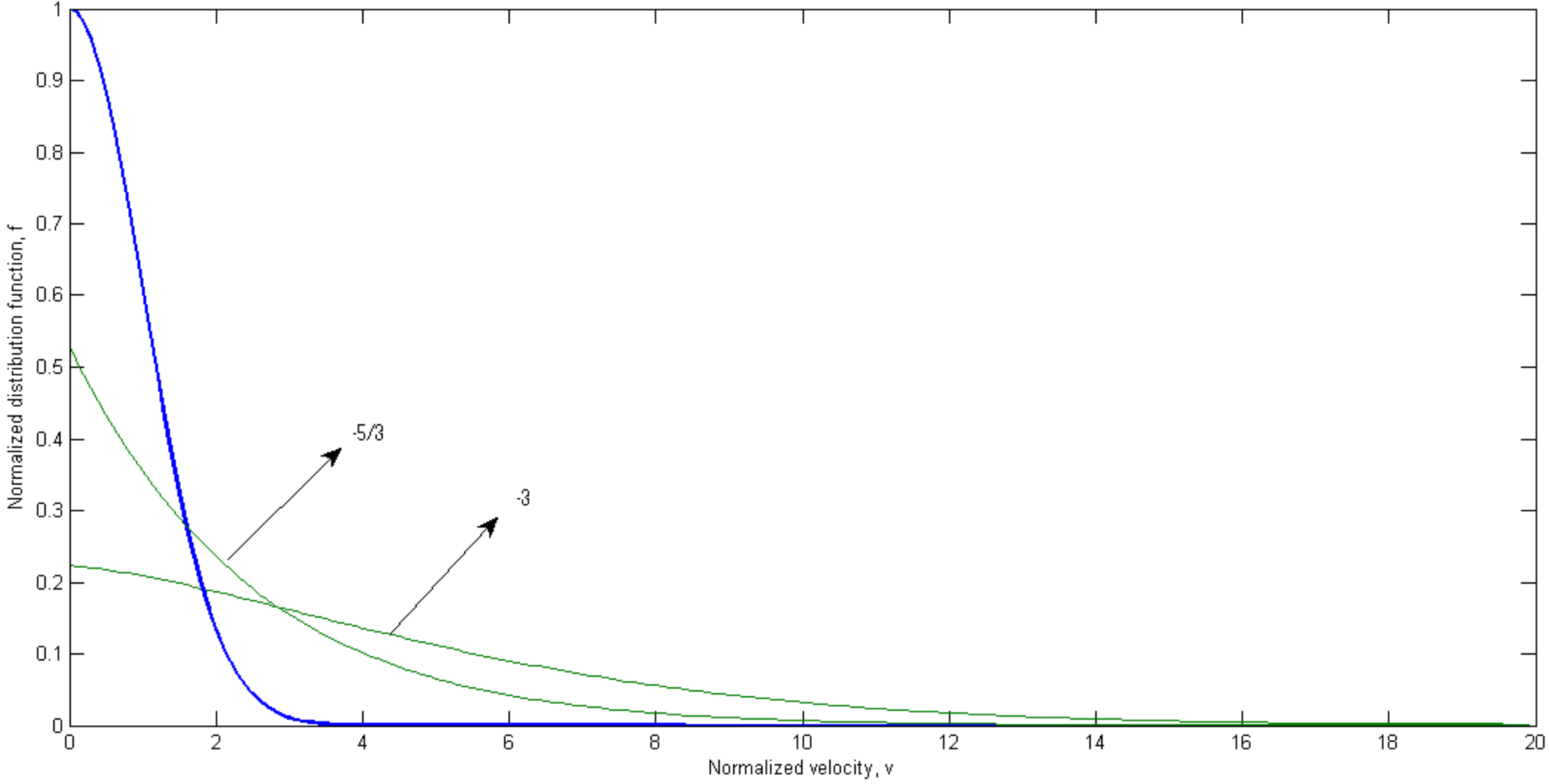
Normalized distribution function, f
Normalized velocity, v
-5/3
-3
0
0.1
0.2
0.3
0.4
0.5
0.6
0.7
0.8
0.9
1
0
2
4
6
8
10
12
14
16
18
20